THE STUDY OF HIGH-SPIN STATES IN ^{196}Hg

BHEKITHEMBA MICHAEL MSEZANE

Thesis presented in fulfillment of the requirements for the degree of Master of Sciences

in the Department of Physics and Engineering

at the University of Zululand

Supervisor: Dr. J.J. Lawrie

Department of Physics

iThemba LABS

Co-supervisor: Prof. O.M. Ndwandwe

Department of Physics and Engineering

University of Zululand

November 2006

DECLARATION

I, the undersigned, hereby declare that the work contained in this thesis is my own original work and that I have not previously in its entirety or in part submitted it at any university for a degree.

Signature: .....

Date: .....

THE STUDY OF HIGH-SPIN STATES IN ^{196}Hg

Bhekithemba Michael Msezane[βαδ]
iThemba LABS, P.O. Box 722, Somerset West, 7129, South Africa

November 2006

ABSTRACT

High-spin states in the oblate deformed even nucleus of ^{196}Hg have been studied by γ-ray spectroscopy following the ^{198}Pt (α, 6n) ^{196}Hg reaction at an incident energy of 65 MeV. The experiment was performed at iThemba LABS using the AFRODITE array. The γ-γ coincidence data in two different experiments using different geometries of the γ-detectors are obtained. The analysis of results, concentrating on the measurement of **D**irectional **C**orrelations in **O**riented (DCO) state ratios and anisotropy polarization lead to extension of the level scheme up to energy E=8.3 MeV and spin I=29ħ. The dipole bands consist of M1 and E2 cross-over transitions were observed at higher excitation energies and spins.

[β] University of Zululand
[α] iThemba LABS
[δ] email: bmmsezane@tlabs.ac.za

ACKNOWLEDGEMENTS

I would like to express my sincere gratitude to the following people for making the realization of this thesis to be successfully:

- Dr J.J. Lawrie[α], for a good supervision, support, encouragement and guidance he gave me throughout the duration of this project. God bless you (*Mnumzane*);

- Dr Elena Lawrie[α], for her willingness to help at all the times, "The role you've played during this project will never be neglected or hidden", Thanks;

- Prof O.M. Ndwandwe[β], my co-supervisor, for allowing me to pursue this research in the Department of Physics and Engineering;

- To all iThemba LABS and University of the Western Cape staff for their support and assistance they gave me throughout the duration of this project;

- To the late Dr. T.K. Marais (may his soul rest in peace), Prof J.F. Sharpey-Schafer[μ] and Prof O.M. Ndwandwe for the initiation of MANUS/MATSCI programme;
- The National Research Foundation (NRF) for the financial support;
- To all the postgraduate students (iThemba LABS and UWC based) for their support and encouragement. *Engithanda ukukusho ukuthi ngifunde okuninginingi sindawonye ngethemba ukuthi kuyongisiza impilo yami yonke;*

This work is dedicated to my family, kumama nakubaba, abafowethu nodadewethu, ngithanda ukubonga ukungisekela nokungibekezelela kwenu, lo msebenzi ubungeke ube yimpumelelo ngaphandle kwenu, benihlale ningikhuthaza ngaso sonke isikhathi uma izinto zinzima noma sengilahle ithemba. Ngiyabonga kakhulu, lo msebenzi ungowenu.

Msezane Bhekithemba Michael (Mashoba) *2006*

[α] iThemba LABS.

[β] University of Zululand.

[μ] Former iThemba LABS director.

TABLE OF CONTENTS

LIST OF FIGURES

LIST OF TABLES

CHAPTER 1 INTRODUCTION

1.1 History of gamma rays

Many physicists gave all credit to the French physicist, Henri Becquerel in 1896 for his discovery of gamma radiation being emitted by Radium-226. Radium-226 is part of the uranium decay chain. Gamma radiation is electromagnetic radiation that takes high quantum energy in the electromagnetic spectrum. Gamma rays are emitted from nuclei of some unstable atoms. They have known to be most energetic photons with short wavelength.

Other properties of gamma-rays

- Gamma-rays are very high energy ionizating radiation; typically gamma-ray photons have about 10 000 times as much energy as the photons in the visible range of the electromagnetic spectrum. It is also noted that there is an overlap between higher energy X-rays and lower energy gammas.
- Gamma rays are photons and have no rest mass, travel at the speed of light and have no electrical charge i.e. they are pure electromagnetic energy.
- Gamma photons are highly penetrating and unlike charged particles, do not lose energy gradually as they pass through matter. Instead the intensity of a beam of photons is attenuated through the loss of photons in single or a small number of interactions. Very dense materials with high Z such as lead are commonly used to shield against gamma photons.

The difference between gamma and X-rays is their origin. Gamma-rays originate in the nucleus whereas X-rays originate in the electron fields surrounding the nucleus. Although gamma radiation (photons) is dangerous to living organisms, it can also be useful. The most common gamma emitters (radionuclides) like Cesium-137, Cobalt-60, etc are used for various reasons but mostly for cancer treatment.

1.2 Overview of mercury-196

The ^{196}Hg nucleus is the lightest stable isotope of mercury. The medium-to-heavy mass mercury nuclei, with *Z=80* having only two protons less than the magic number 82, are weakly oblate deformed in the ground states and up to moderate excitation energies. The shape of a nucleus is said to be *oblate* (pumpkin shape) when two of its principal axes have the same length, and the third axis is shorter. For an *oblate* nucleus, the intrinsic quadrupole moment (Q_0) is negative. Their energy level schemes display sequences of states that are connected by strong *E2* transitions. Negative-parity bands have been observed in these nuclei starting from $I^{\pi}=5^{-}$. The level schemes are interpreted as bands of collective rotation of the oblate nuclei around an axis perpendicular to their symmetry axes. The band structures give test cases for application of the *Cranked Shell Model* (CSM) to oblate nuclei. The routhians, band crossing frequencies and aligned angular momenta calculated within the framework of CSM agree with the experimental results [MEH91].

1.3 Previous studies in ^{196}Hg

There are many different publications about the study of ^{196}Hg [PET68, PRO74, GUT83, HEL83, KRO81, and MEH91] concentrating on the extension of level scheme.

The investigation carried by Petry *et al.* [PET68], deduced the level schemes of even mercury isotopes including ^{196}Hg as shown in fig 1.1a. The first six levels were placed in parallel with that of ^{194}Hg except for the 6^{+} level at excitation energy E=1785 keV. The level scheme [PET68] was built on the ground state band of even-even nucleus up to 6^{+} and 7^{-} states, where transition 723.6 keV was assigned to be tentative. Unfortunately in that work, the statistics were too poor to make any statement about coincidence relationship with either the 426 or 635.5 keV. Hence, the spins and parities suggestions for these levels were made based on β-decay selection rules and measured γ-ray multipolarities.

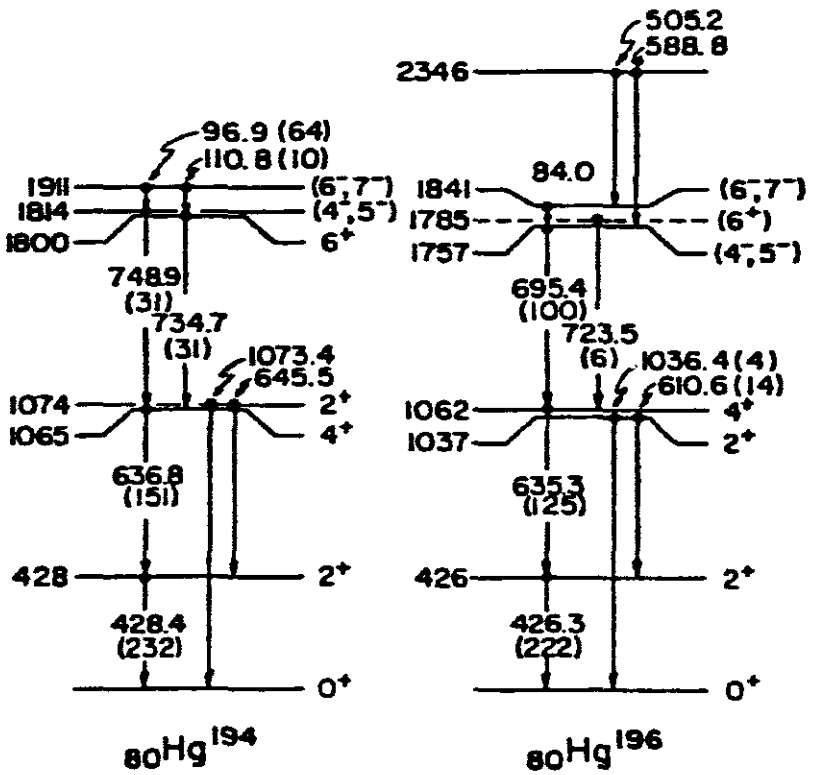

Fig 1.1a: Partial level scheme for ^{194}Hg and ^{196}Hg from [PET68].

Proetel *et al.* [PRO74], observed γ-ray decay of the yrast states of ^{196}Hg using the ^{196}Pt(α,4n) ^{196}Hg reaction with a 5 mg/cm^2 target thickness. The energy level scheme proposed by [PET68] was confirmed and then extended up to around spin I=12 for both the positive- and the negative-parity bands. Nanosecond isomeric states were measured at $I^{\pi}=10^+$ and $I^{\pi}=7^-$ from time spectra in that work.

The study carried by Kroth *et al.* [KRO81], concentrated on identification of the missing rotation-aligned ($\nu_{i_{13/2}}^{-2}$) 12^+ state in ^{196}Hg. In their investigation, excited states of ^{196}Hg were populated with (α,2n), (α,4n), and (d,3n) reactions in which metal foil targets were bombarded with 30 and 48 MeV alpha particles and 22 MeV deuteron beams. Two transitions (79 and 96 keV) were observed above 4^- levels in the ground state band. The

96 keV γ-ray has previously been assigned as the $10^+ \rightarrow 8^+$ transition [PRO74] whereas the 79 keV γ-ray has not been observed earlier. A careful study of time spectra indicated the existence of two isomeric states above the 8^+ level, and allowed them to conclude that, the 79 keV line is the $10^+ \rightarrow 8^+$ isomeric transition. In addition to the revised level scheme, at $I^\pi=10^+$ they have added two new levels at 2143 keV and 3507 keV. Other transitions in ^{196}Hg with energy $E_\gamma(I_\gamma)$=278.4 keV(22), 386.1 keV(13), 412 keV(9), and 690.4 keV(9) could not be placed in the level scheme.

Another investigation carried by Guttormsen *et al.* [GUT83], confirmed the 96 keV $12^+ \rightarrow 10^+$ transition and the 79 keV $10^+ \rightarrow 8^+$ transition in ^{196}Hg. They also confirmed the 278 keV $10^+ \rightarrow 9^-$ transition which were previously assigned tentatively. Apart from the additional new observed transition in Kroth's work, the transition $8^- \rightarrow 7^-$ observed by Guttormsen is different from the one observed by Kroth which is 217.2 keV and 301.0 keV respectively.

Helppi *et al.* [HEL92], reported results of a study of levels in ^{196}Hg by the reaction ^{196}Pt(α,4n) at E=48.6 MeV. The level scheme was extended up to 18^+ and 21^- level; however, they were unable to find evidence for the proposed 278 keV $10^- \rightarrow 9^-$ transition [KRO81, and GUT83]. They observed no trace of a 217 keV γ-ray in ^{196}Hg but as for 301 keV $8^- \rightarrow 7^-$ proposal, they find mutually coincident 300.5 and 301.5 keV γ-rays in ^{196}Hg, however neither of these transitions is coincidence with 84 keV $7^- \rightarrow 5^-$ transition. The level scheme observed by Mehta *et al*, has got many newly observed transitions.(see fig 4.8). Cederwall *et al.* observed a dipole band at higher energy and spin.

1.4 Overview of the Cranked Shell Model (CSM)

The cranked shell model is the most useful model for high-spin state calculations. The cranked shell model was introduced by Inglis in 1954 [ING54], and further developed by Bengtsson and Frauendorf [BEN79]. The model was first applied to mercury (Hg) isotopes by Guttormsen and Hübel [GUT82]. The full details of cranked shell model theory and formulism are given in many textbooks such as [NIL95].

The model gives a fully microscopic description of the influence of rotation on single-particle motion. At very high spins, when the Coriolis and centrifugal forces strongly perturb the wave function of many nucleons, better description of the single-particle energies is obtained through the CSM [ING56]. The Coriolis force acts to align the angular momentum of the nucleons with the rotation axis.

In the cranked shell model, the rotation is treated classically with the rotation vector coinciding with one of the main axes of the nucleus. The nucleons can then be described as independent particles moving in a rotating potential well, where the intrinsic coordinate frame has a fixed rotational frequency ω.

The single-particle cranking Hamiltonian was originally derived by transforming the time-dependent Schrödinger equation from the space-fixed coordinate system to an intrinsic body-fixed system in which the deformed nuclear potential is static. The single-particle cranking Hamiltonian is given by

$$h^{\omega} = h^{0} - \eta\omega j_{x} \qquad 1.1$$

where h^0 is the Hamiltonian in the laboratory system, j_x is the projection of the total angular momentum operator onto the rotation axis, and the term $-\hbar\omega j_x$ contains the Coriolis and centrifugal terms, which modify nucleon orbitals. The Schrödinger equation in the rotating system can be solved in the standard way as an eigenvalue problem. The eigenvalues of the Hamiltonian are known as Routhians. The total cranking Hamiltonian can be obtained by summation over all of the independent particles of the system,

$$H^{\omega} = H^{0} - \eta\omega I_{x} \qquad 1.2$$

where I_x is a projection of the total angular momentum onto the rotation axis.

The cranking Hamiltonian can be modified by including a pairing term that is given by,

$$H^{\omega} = H^{0} - \eta\omega I_{x} - \Delta\left(P^{+} + P\right) - \lambda N \qquad 1.3$$

where Δ is the pair gap, and P^+ and P are the quasi-particle pairing creation/annihilation operators. The total number of particles is kept constant by introducing the Fermi

surface term $-\lambda N$. The Hamiltonian is known as the Hartree-Fock-Bogolyubov (HFB) Hamiltonian and calculations using this Hamiltonian give *quasi-particle Routhians.*

1.5 Compound-nucleus reaction

The heavy ion induced fusion-evaporation reaction is the most commonly used way of producing nuclei at high excitation energy and high angular momentum. The reaction occurs when the projectile nucleus has an impact parameter smaller than the radius of the target nucleus. The projectile nucleus will enter the target nucleus, and its nucleons will interact of the target nucleons through simple scattering processes.

By successive nucleon-nucleon collisions within the combined system of the projectile and the target nucleus, the energy of the projectile is continuously shared among the nucleons until an equilibrium state is reached. The average increase in the energy of any single nucleon is not enough for it to escape from the nucleus, but due to some successive random collisions, there is a statistical distribution of energy so that there is a probability that a nucleon will obtain sufficiently energy to escape from the nucleus.

The process results in the formation of a compound nucleus, which is the intermediate stage after the absorption of the projectile nucleus but before the emission of outgoing particles. The schematic diagram in fig 1.1 shows the process. Fusion-evaporation reactions are considered to proceed in two independent stages:

i. The formation of compound nucleus and
ii. Decay of the compound nucleus by evaporation of light particles

The following are the characteristics of a compound nucleus reaction between a small projectile and the larger target nucleus:

- The theory of compound-nucleus model is applicable for low incident energies ranges in MeV/nucleon (up to ~10 MeV/nucleon for heavy ion induced reaction), because of low probability that the incident particle will escape from the nucleus with its identity and its energy intact.

- Due to the random nature of interactions among the nucleons, one may expect that the evaporation particles are emitted isotropically in the centre of mass system.
- The higher the excitation energy of the compound nuclei, the more particles are likely to evaporate, and therefore the analogy 'evaporation' is appropriate for the compound-nucleus model. This is illustrated in fig 1.2.

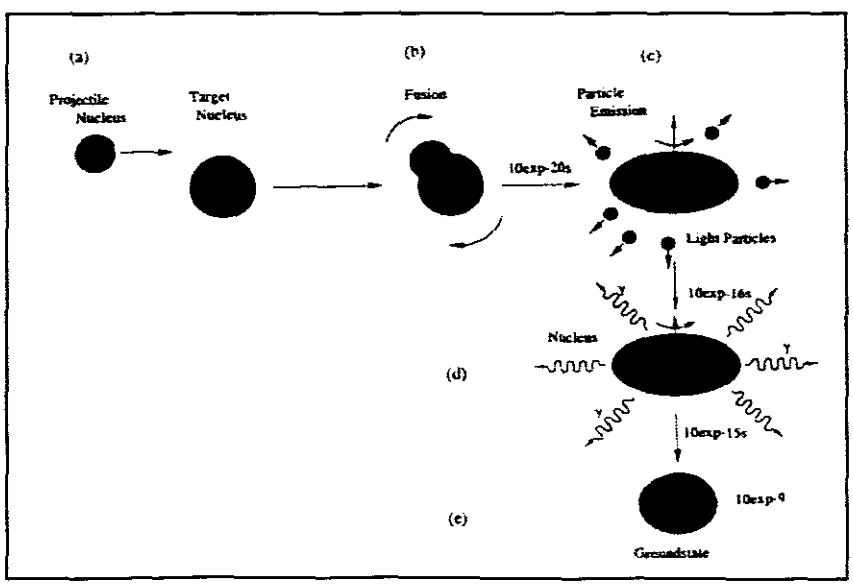

Fig 1.2: shows the formation and decay path of compound nucleus.

Charged particle (proton, alpha particles) emission is normally suppressed by the Coulomb barrier; therefore the compound nucleus will be more likely to emit a neutron than a charged particle. However, for highly neutron deficient compound nuclei, more energy will be required to remove neutrons than protons or alpha particles, hence alpha particle evaporation along with neutron evaporation forms a large part of the fusion-evaporation cross-section.

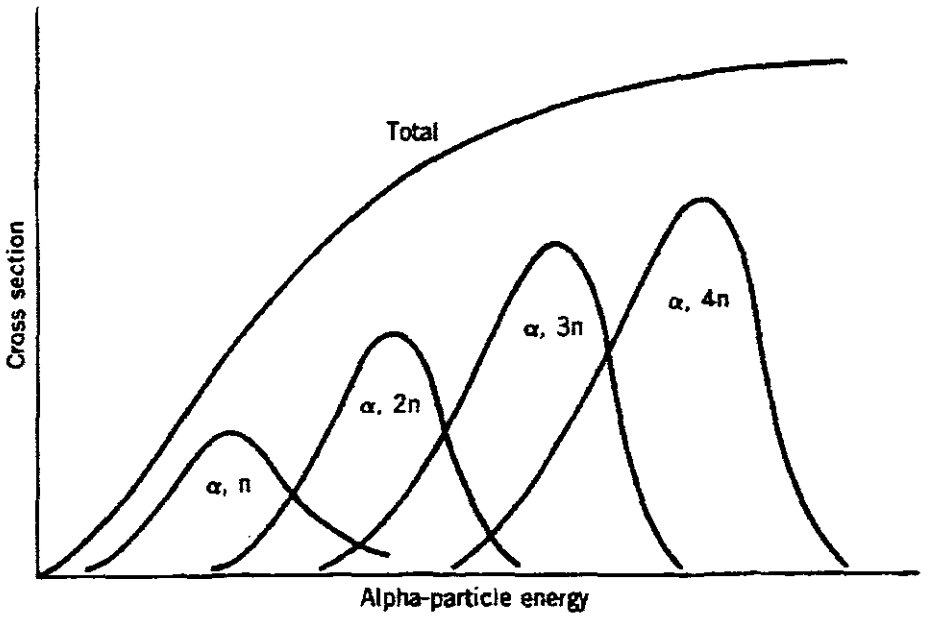

Fig 1.3: *The cross-section of (a,xn) reactions as a function of the incident energy. Each cross-section exhibit a Gaussian-like shape which has a maximum at alpha particle energy that increases with the number of evaporating neutrons [KRA88].*

Later the excited residual nucleus decays to the ground state by the emission of gamma quanta. The emitted gamma quanta may be divided into statistical and yrast cascades as shown schematically in fig 1.3 where the upper thick line represent the high angular momentum entry region for a heavy projectile producing residual nuclei in the mass region A~160. The statistical γ-rays are high energy (several MeV) dipole transitions. These γ-rays carry away large amounts of excitation energy and small amount of angular momentum.

According to the Neils Bohr [LIL01] independence hypothesis, the formation of a given compound nucleus may be due to many different reactions, but the probability of populating a final state of the residual nucleus is independent of the formation process of the compound nucleus, and only depends on the amount of excitation energy available.

The yrast line is defined as the sequence of states with the lowest possible energy for a given angular momentum. The yrast line is approximately ~ 8 MeV below the particle evaporation threshold. Gamma-rays in the yrast region are emitted with lower energy but

higher angular momentum than in the statistical region. The yrast-like transitions are of interest to the γ-ray spectroscopist because they can clearly reveal the properties of nucleus [GRE99].

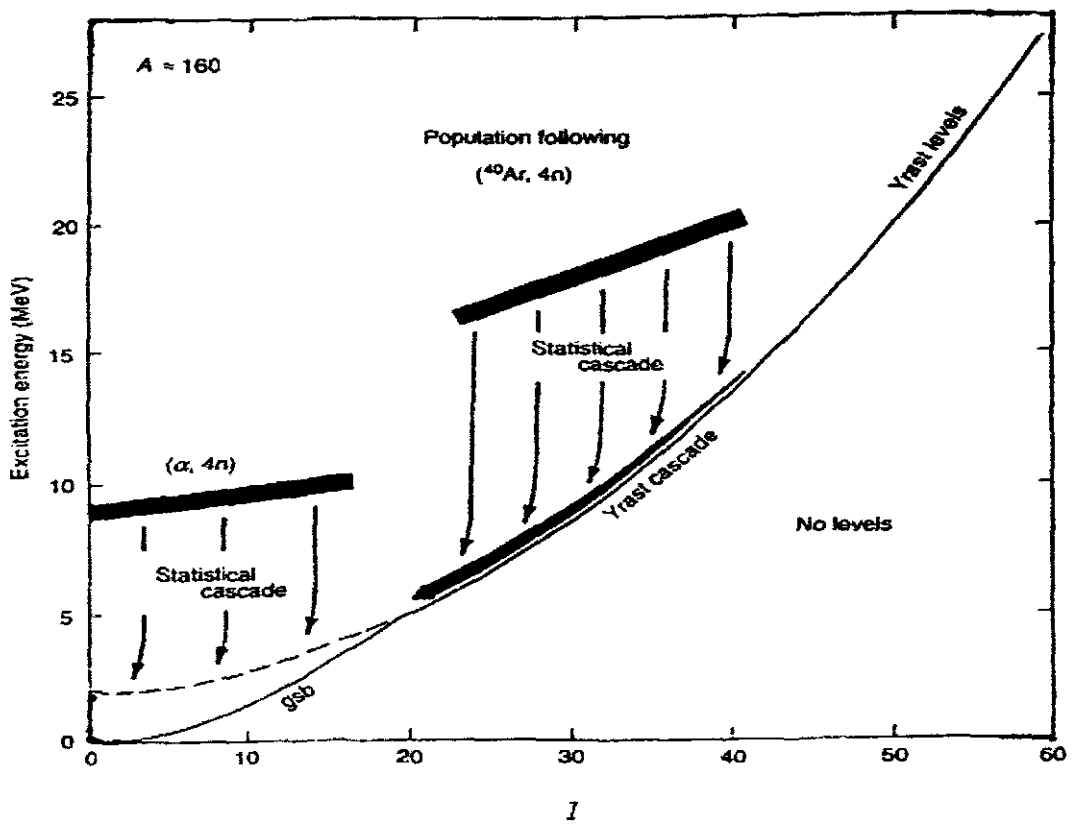

Fig 1.4: A schematic diagram of excitation energy as angular momentum in the A≈190 region indicating statistical and yrast cascades after (a,4n) and (^{40}Ar,4n) reactions [NIL95].

1.6 Aim of this study

The initial purpose of this experiment was to calibrate the AFRODITE array for the measurement of lifetimes with the Recoil Shadow Anisotropy Method (RSAM) using the lifetime of known isomers [GUE04]; however the experiment also yielded new data on excited states in ^{196}Hg. The main aim of this project is to study high spin states in ^{196}Hg that were populated in the ^{198}Pt (α,6n) reaction at an incident energy of 65 MeV.

Although this is the same reaction used by Mehta *et al.* [MEH91] the present experiment was done with a substantially larger array of γ-detectors allowing the observation of weaker transitions. This study will focus on the determination of spins and parities of newly observed levels as well as of levels for which previous assignments were tentative. This is done by measuring Directional Correlation of Oriented states (DCO ratios) in order to determine the multipole order of gamma transitions, and by measuring linear polarization from Compton scattered events in the clover detectors. Polarization (Anisotropy) is measured from the asymmetry between vertical and horizontal Compton scattered events and can be used to distinguish between electric and magnetic transitions.

The rest of the thesis is organized as follows; chapter 2 gives full details of experimental techniques and equipments that are going to be used in this project. Experimental data analysis is given in chapter 3 which concentrates in DCO ratio and anisotropy measurements. The experimental results and discussions will be given in chapter 4. In chapter 5, conclusion and outlook will be presented.

CHAPTER 2 EXPERIMENTAL TECHNIQUES AND EQUIPMENT

2.1 Interaction of γ-rays with matter

There are several ways in which γ-rays interact with matter. The way in which γ-rays and X-rays behave greatly differs from that of charged particle. The difference is due to the fact that X-rays and γ-rays are uncharged and therefore do not interact with the Coulomb field of the atomic electrons. As a result they are many times more penetrating than charged particles. It is important to know how γ-rays interact with matter through the three dominant processes namely; the photoelectric effect, Compton scattering, and pair production, since these processes determine the response of detectors to γ-rays.

2.1.1 Photoelectric effect

The Photoelectric effect involves the absorption of the energy of the incident photon by an atomic electron in the absorber material. Most of the energy of the γ-ray is transferred to the electron, which is ejected from the atom, leaving it in an excited state. The photoelectron is ejected with a kinetic energy given by:

$$T_e = E_\gamma - B_e \qquad 2.1$$

where B_e is the binding energy of the electron. The excited atom from which the electron was ejected will subsequently capture an electron to fill the hole and will de-excite to the ground state by emitting X-rays. The photoelectric absorption is dominant for low energy photons (< 200 keV) [MCC84]. The interaction depends upon atomic number Z with the absorption cross-section being approximated as:

$$\sigma \propto Z^n \qquad 2.2$$

where n is normally between 4 and 5 depending on the absorber material. The dependence explains the choice of high-Z material for shielding purposes and for use in γ detectors.

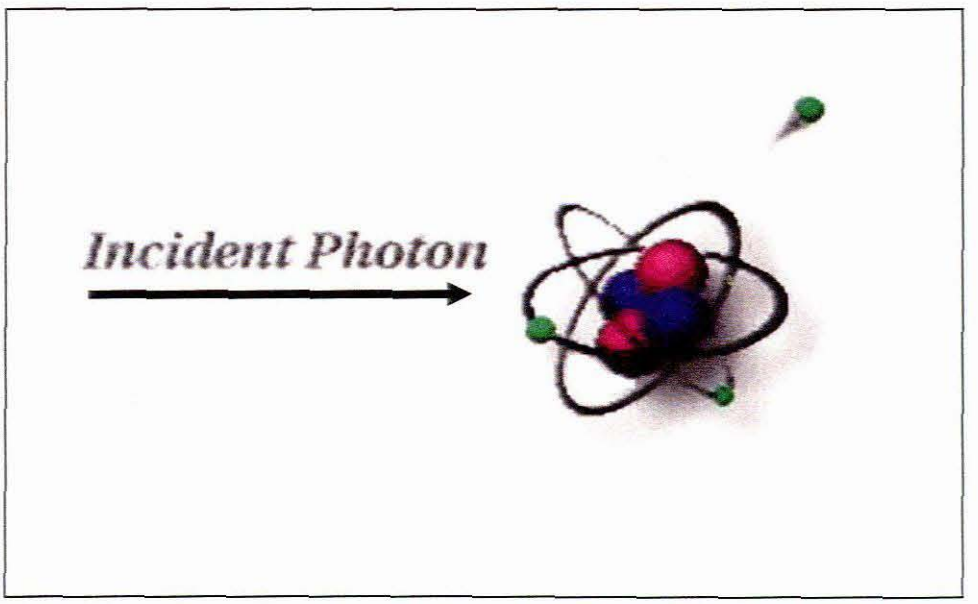

Fig 2.1: illustrates the Photoelectric Effect process [NDT00].

2.1.2 Compton scattering

This process is illustrated in fig 2.2. It is known to be the best understood process in photon interactions. The Compton scattering process takes place between the incident γ-ray photon and an electron in the absorber material. During the Compton scattering process, an incident γ-ray photon interacts with an atomic electron and is deflected through at an angle θ with respect to the original direction. In this process the photon transfers part of its energy and momentum to the electron (assumed to be at rest before the interaction). The electron, known as a recoil electron, is ejected from the atom leaving it in an excited state.

The expression which relates the energy transferred and the scattering angle are derived from the principle of conservation of energy and momentum simultaneously as:

$$E'_\gamma = \frac{E_\gamma}{1+\frac{E_\gamma}{m_0c^2}(1+\cos\theta)} \qquad 2.4$$

where E_γ is the incident energy, E'_γ is energy of the scattered photon at an angle θ and m_0c^2 is electron rest mass energy (0.511 MeV). Energy transferred always depends on the scattering angle *i.e.* for small θ very little energy transferred. From equation 2.4, the maximum energy transfer to the electron occurs at $\theta=\pi$.

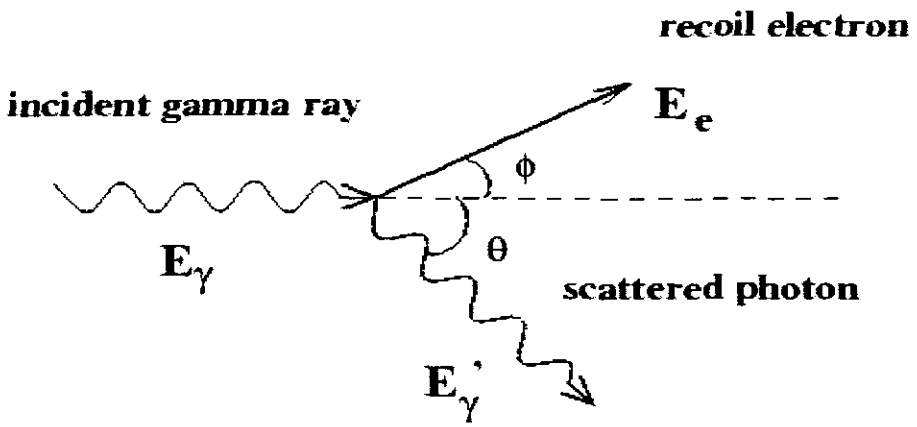

Fig 2.2: illustrates Compton scattering process

Compton scattering is most probable in the 200-1000 keV energy range and the probability decreases rapidly with increasing energy. The probability of Compton scattering per atom depends on the number of electrons available as scattering targets and therefore increases linearly with Z [KNO99].

2.1.3 Pair production

The pair production process is illustrated in fig 2.3. This process occurs only if the gamma-ray energy exceeds twice the rest-mass energy of an electron (1.022 MeV). The process of pair production involves the transformation of a photon into an electron-positron pair as primary products. The process takes place in the vicinity of the nuclear

field of the nucleus. Above the 'threshold' (1.022 MeV) energy, probability for pair production increases steadily with increasing energy. Excess photon energy over the threshold is converted into kinetic energy shared by the positron and electron.

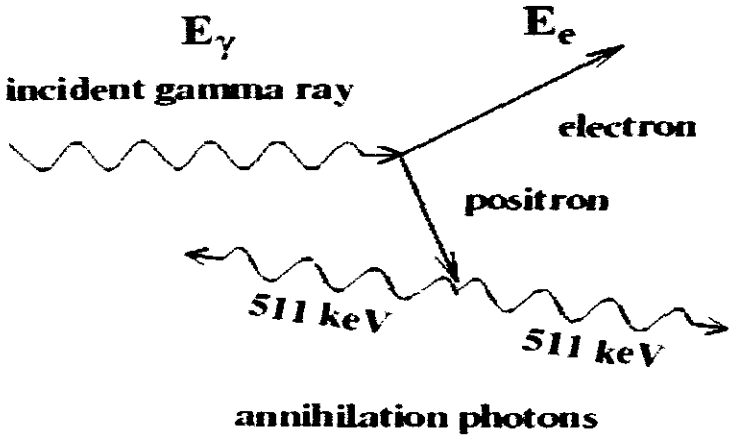

Fig 2.3: illustrates Pair Production process

The positron is slowed down due to the energy loss through the interactions with atomic electrons in the surrounding medium. After coming to rest the positron annihilates with an electron to form two annihilation photons each having energy of 0.511 MeV as secondary products. The two annihilation photons are emitted in opposite direction to each other for conservation of momentum.

Figure 2.4 illustrates the different regions for all three major types of gamma-ray interaction with matter. The graph shows how each interaction depends on energy and Z of an absorber.

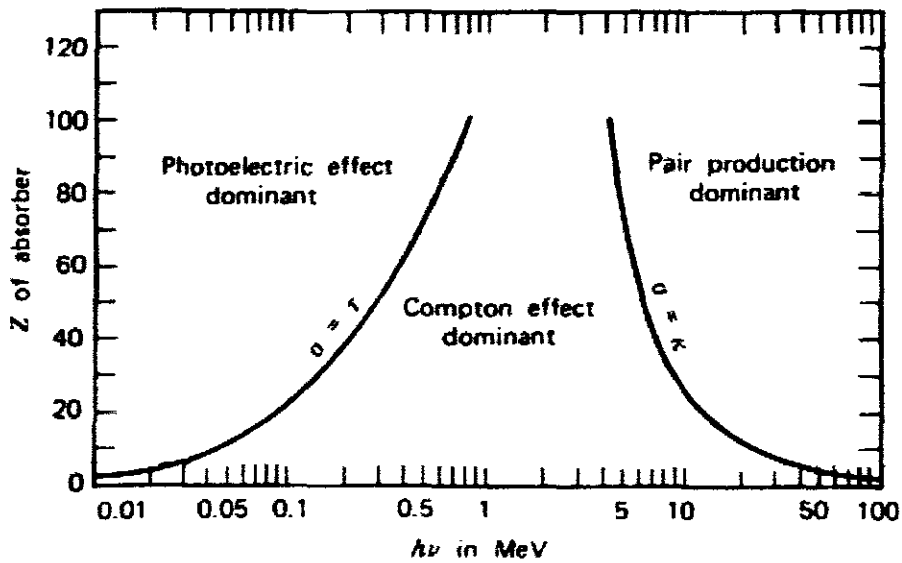

Fig 2.4: illustrates different regions where each of gamma-ray interaction dominates.

2.1.4 Attenuation

The three interaction processes described above cause a well collimated photon beam to be attenuated. The photon may undergo photoelectric absorption or pair production where it disappears altogether or Compton scattering where it is deflected away from a detector placed at forward direction.

The dependence of photon intensity on absorber thickness is most easily calculated in a well-collimated beam. Consider a beam of intensity I photons per second, incident on a thin section (thickness *dx*) in a slab of material whose atomic density is N. If the total interaction cross section per atom of material is σ, the rate of removal of photons from the beam is given by:

$$dI = -N\sigma I dx \qquad 2.9$$

The total cross-section has contribution from all three interaction processes.

$$\sigma = \sigma_{pe} + Z\sigma_{c} + \sigma_{pp} \qquad 2.10$$

where σ_{pe} and σ_{pp} are atomic photoelectric and pair production cross-sections respectively, and σ_c is the Compton scattering cross-section for a single electron as illustrated in fig 2.5 [LIL01]. Equation 2.9 leads to the transmitted intensity passing through a thickness t being given by:

$$I = I_0 e^{-\mu t} \qquad 2.11$$

where μ represent attenuation coefficient and t is a thickness of the material.

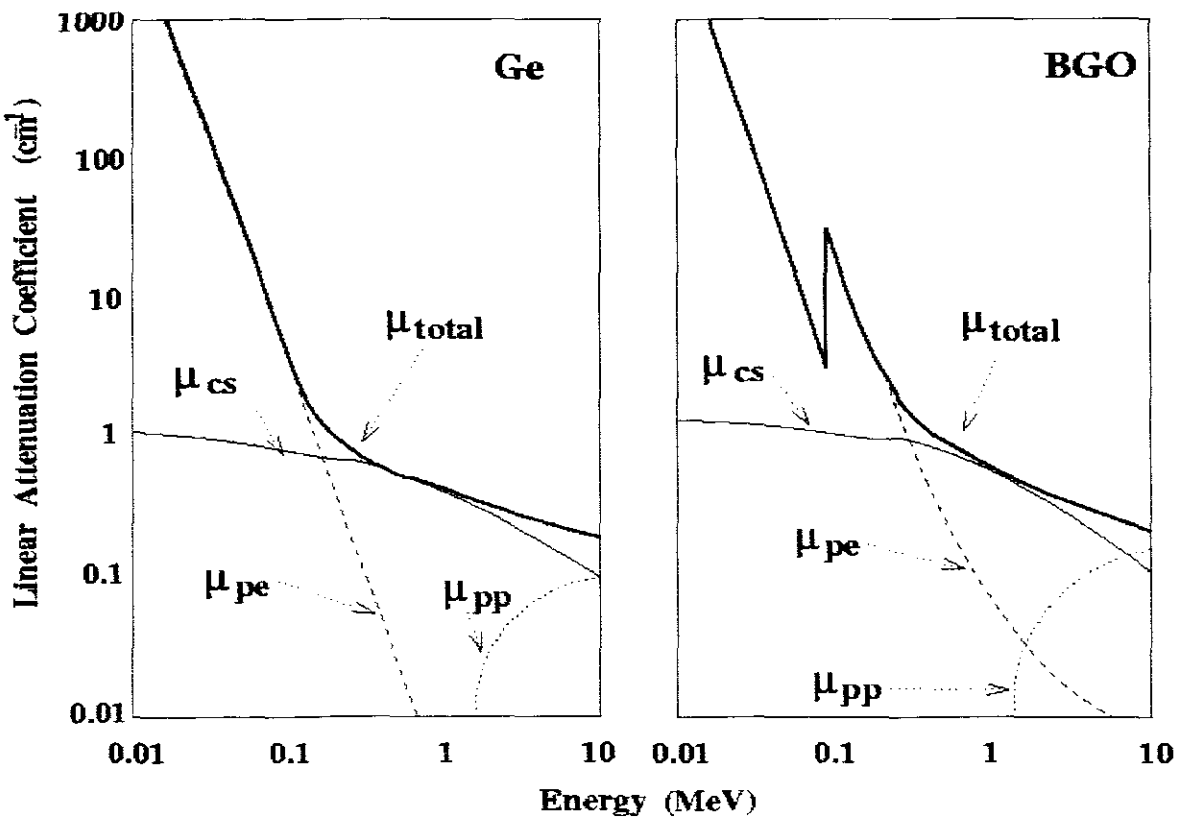

Fig 2.5: shows the linear attenuation coefficient of both Ge and BGO.

2.2 Experiment equipment

In order to study high-spin states in nuclei, the following equipment are usually used:

- Accelerator to produce the desired accelerated projectile particles.
- Beam lines to deliver the beam to the target.
- Appropriate reactions to produce the nuclei of interest with sufficient reaction rates and
- Detectors with high γ-rays efficiency and good resolution.

2.2.1 Overview of iThemba LABS facility

The iThemba Laboratory for Accelerator Based Science (LABS) is located at Faure, 30 km away from Cape Town, South Africa. Currently there are four particle accelerators in operation at the laboratory, two solid pole cyclotrons, a separate-sector-cyclotron (SSC), and a 6 MV Van der Graaff accelerator. The Van der Graaff accelerator is mostly used to study material science. The large k-200 SSC (having dimensions of 13.2 m in diameter and 7 m in height) can accelerates protons up to 200 MeV, and heavier particles to much higher energies.

The accelerated charged particles are fed to the SSC via one of the two smaller solid-pole injector cyclotrons that is able to accelerate proton up to 8 MeV. One of the injectors provides intense beams of light ions and is used for radio-isotope production and radio therapy.

The second injector accelerator has external ion sources that provide polarized protons and heavy ions beams such as krypton, argon and carbon. The schematic layout of beam lines are shown in Fig 2.6 and the definition of symbols are also given in table 2-1.

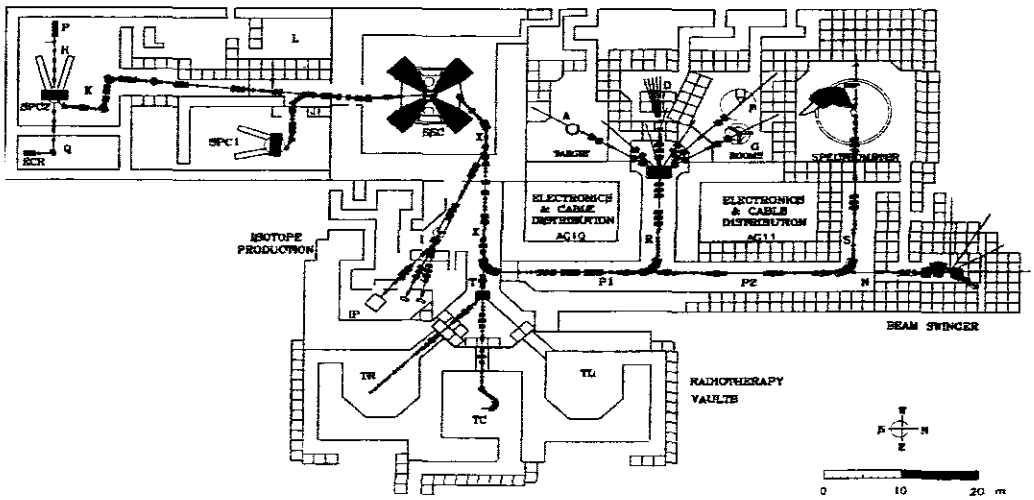

Fig 2.6: shows the layout of beam at iThemba LABS.

Table 2-1: gives the descriptions for the abbreviations used in iThemba LABS layout.

Abbreviation	Description Details
A	Scattering chamber beam line
D	Collimated neutron beam facility
ECR	Electron Cyclotron Resonance ion source
ECD	Electron and Cable Distribution
F	High-energy gamma-ray detectors (AFRODITE array)
G	Gamma-ray angular correlation table
IP	Isotope production facility
L	Low-energy experimental area
P	Polarized-ion source
SPC1	Solid-pole injector cyclotron for light ions
SPC2	Solid-ion cyclotron for heavy and polarized ions
SSC	Separated-Sector Cyclotron
TC	Isocentric system for neutron therapy
TR	Horizontal beam line for proton therapy
TL	Beam lines for proton

2.2.2 AFRODITE array

AFRODITE, an acronym for the AFRican Omni-purpose Detector for Innovative Techniques and Experiments, was commissioned at iThemba LABS (previously known as National Accelerator Centre (NAC)) early in 1998. The AFRODITE array is used to detect both X- and γ-ray energies *i.e.* low and high energy photons, with high efficiency. The AFRODITE array-frame, has a rhombicuboctahedron shape (see figure 3.1), with a total of eighteen square facets at 45, 90, 135 degrees with respect to the beam direction. Although in principle sixteen square facets can be accommodated only fifteen of these can be achieved since the top most square facet, positioned at 90° with respect to the beam direction, is used to support the hydraulic target ladder positioner [NEW98]. There are two types of High Purity Germanium (HPGe) γ-ray detectors that are being used in the array, namely the eight composite Clover detectors and eight Low-Energy Photon Spectrometers (LEPS).

The clover detectors are each housed inside a symmetric Bismuth Germinate ($Bi_4Ge_3O_2$ or BGO) suppression shield as discussed in section 2.2.6 (Compton suppression). The purpose of the BGO is to reject events in which incident γ-rays interacting in a clover are Compton scattered out of the detector, thus enhancing the ratio of full-energy to partial-energy events (called the peak-to-total, (P/T) ratio).

For an ideal radiation energy detector, the most important requirement factor is the energy resolution. The energy resolution is measured by determination of the FULL WIDTH at HALF MAXIMUM (FWHM) of the photopeak, for mono-energetic γ-radiation. The relative resolution at a given energy E is given by $\delta E/E(\%)$, where δE is the FWHM at energy E. The relative energy resolution, for the clover detectors, is about 1 keV at 350 keV.

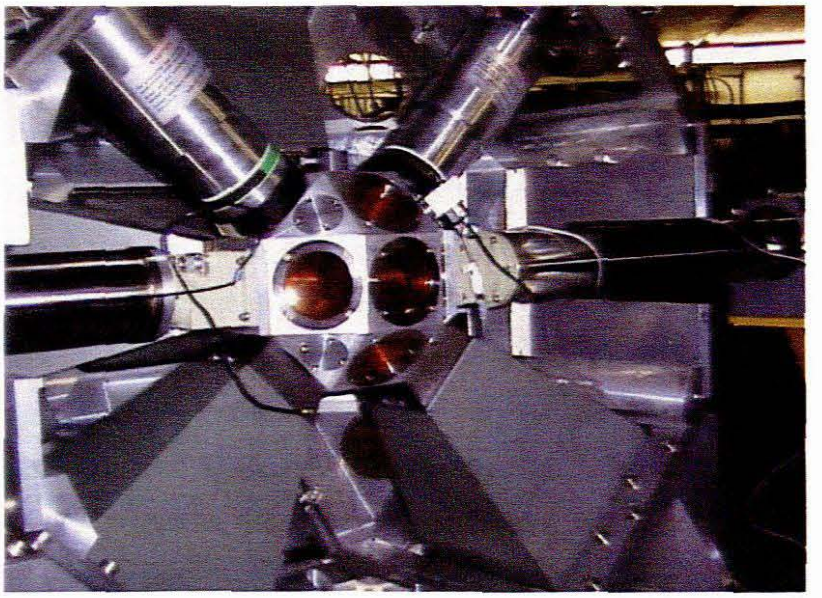

Fig 2.7: *shows the AFRODITE array with kapton windows on the 16 square faces.*

2.2.3 Germanium detectors

Germanium detectors are large reverse biased p-n junction diodes. In order to function as a good γ-ray detector the material must have a high absorption coefficient; this can be provided by a material of high atomic number to enhance the photoelectric cross section. It must also have the low band gap for conduction to occur and must also have low level of impurities thus germanium, is superior to silicon. At a junction between n- and p-type materials, the electrons from n-type material can diffuse across the junction to p-type material and combine with the holes. The charge carriers neutralized and give rise to a region of net zero charge. This region is known as a depletion region (d) which depends on both the reverse bias voltage applied and concentration of germanium impurity as,

$$d \approx \left(\frac{V}{N}\right)^{1/2} \qquad 2.12$$

From this equation it can be seen that decreasing the impurity concentration N will result in an increasing in the size of depletion region. High purity germanium (HPGe) has an impurity concentration of around one in 10^{12} atom which allows a depletion region of several centimeters to be achieved.

The net positive charge on one side of the junction, and net negative charge on the other side set up an electric field gradient across the depletion region. The γ-rays interact with germanium as discussed in section 2.1 to produce electron-hole pairs in the depletion region, which will then be swept to the edges of the detector due to the presence of electric field gradient, constituting the electric current. The minimum energy required for creating an electron-hole pair in germanium is approximately ~ 3 eV as opposed to ~5 eV in Si. The larger number of electron-hole pairs produced per MeV in Ge give rise to better energy resolution. Germanium detectors have to be operated at liquid nitrogen temperature of 77 K to reduce thermal excitation of electrons.

2.2.4 Clover detector

Clover detectors consist of four separate n-type coaxial HPGe crystals which are arranged about 0.2 mm apart as shown in fig 2.8 [JON98]. Four crystals with dimensions of 70 mm in length and 50 mm in diameter each, are housed in the same cryostat (see fig 2.9). In order to achieve maximum close packing, the crystals were tapered over 36 mm from the front face giving a 41x41 mm squire front face. Each clover crystal element has it own associated electronics and signals are processed independently. The resulting high granularity of these detectors allow more accurate Doppler correction and decrease Doppler broadening effects, thus improving energy resolution in experiments where recoil reaction products are not stopped in the target. The close geometry of the four crystals also allow for the process of add-back, where by partial energies, e.g. from Compton scattering events in adjacent element, can be added to reconstruct the full energy. Generally only vertical and horizontal scattered double hit events are included in the add-back (e.g. element 1 and 2 or 2 and 3 in fig 2.8), while diagonal or 3 hit events are assumed to come from more than one incident γ and are ignored. While the relative efficiency of each element is ~23% the total relative efficiency with add-back is ~130%. Add-back also improves the peak-to-total ratio. Therefore clover detectors are ideal for detecting high energy gamma-rays because of their high total photo peak efficiency and high resolving power.

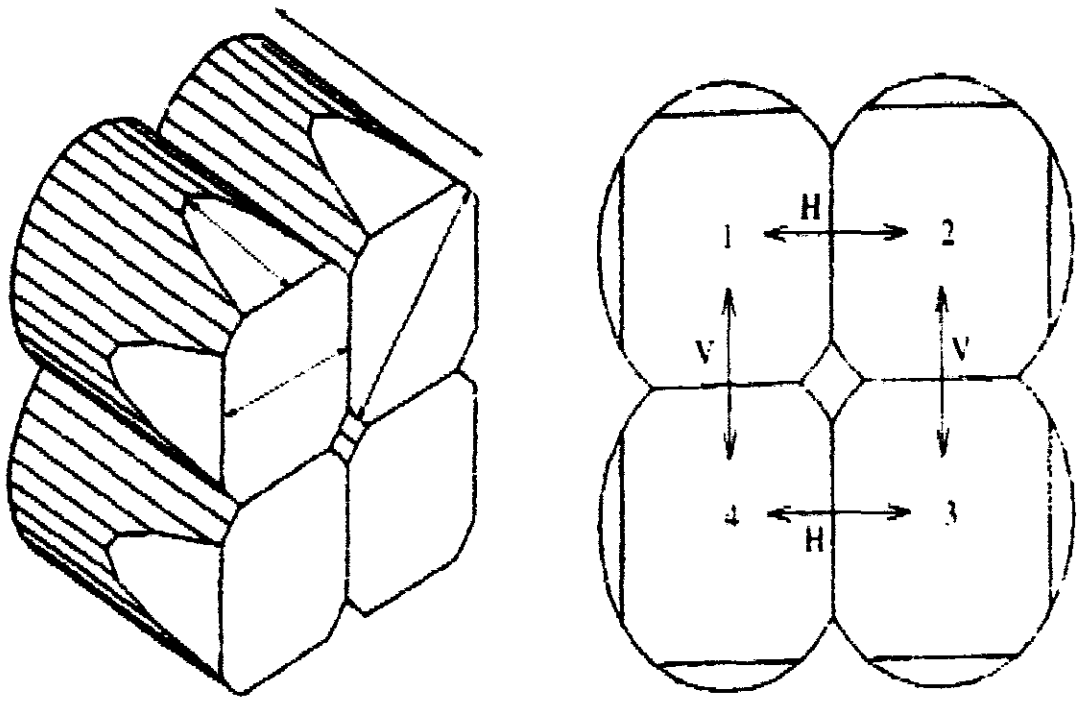

Fig 2.8: shows four separate n-type coaxial HPGe crystals [JON98].

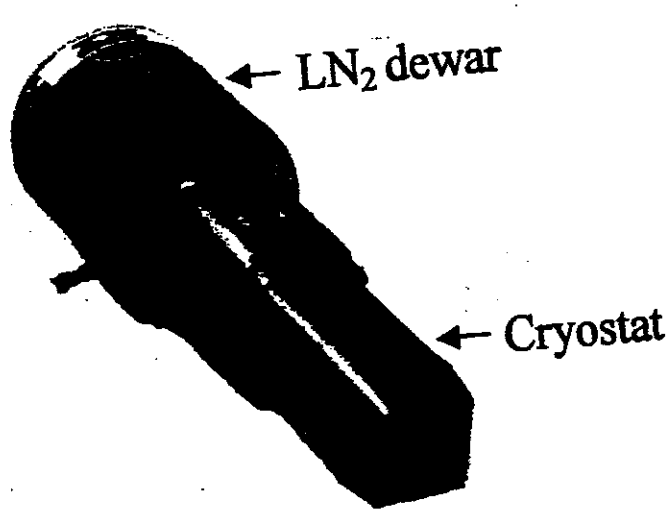

Fig 2.9: shows clover detector coupled by LN_2 filling system

2.2.5 LEPS detectors

The Low-Energy Photon Spectrometer (LEPS) detector is important for the measurement of low energy photons. The LEPS detectors consist of single p-type HPGe crystals in a planar geometry that are electrically segmented into four quadrants [VYM03] with the dimensions of 10 mm thick and 60 mm diameter. The spectrum from each quadrant is processed separately. Some important specification of the AFRODITE array for LEPS is given in Table 2-2 [NEW98]. The LEPS detectors have better energy and time resolution at low energies, but the efficiency drop very rapidly with in creasing energy. They are thus only useful for γ-energies below ~ 200-300 keV.

Table 2-2: shows other important specifications of both clover and LEPS detectors.

Specification	Clovers	LEPS
Supplier	Eurisys	Eurisys
Number at the AFRODITE	8	8
Total opening angle[a]	23.2°	28.3°
Solid angle per detector[b]	1.34%[c]	1.57%
D_{tc}[a]	196 mm	119 mm
D_{ec}	20 mm	15 mm

Definition of superscripts:

a for a 4 mm gap between target chamber and end-cap,

b for the percentage of 4π, and

c for a 0.2 mm distance between crystals.

D_{tc} – the distance from crystal surface to the target center.

D_{ec} – the distance from the detector end-cap to the crystal surface.

2.2.6 Compton suppression

Compton suppression is a technique that improves the signal-to-background ratio by reducing unwanted events where the full γ-ray energy is not observed due to Compton scattering out of the detector. A high resolution gamma-ray detector, like germanium, is surrounded by a high efficiency inorganic scintillator detector to detect the escape scattered gamma-rays. The two detectors are operated in an anti-coincidence mode, so that events that occur at the same time in both detectors are rejected. Both NaI and BGO have been used for this purpose but BGO has a strong advantage in detection efficiency over NaI because of its high density (~7.3 g/mc^3) and atomic number (Z). BGO also has excellent timing properties. The typical example of the pyramid like shape of BGO Compton suppression shield is shown in fig 2.10. Figure 2.10 also shows the

tapered heavy metal collimator with a 35 mm by 35 mm entrance window for gamma rays at the front end.

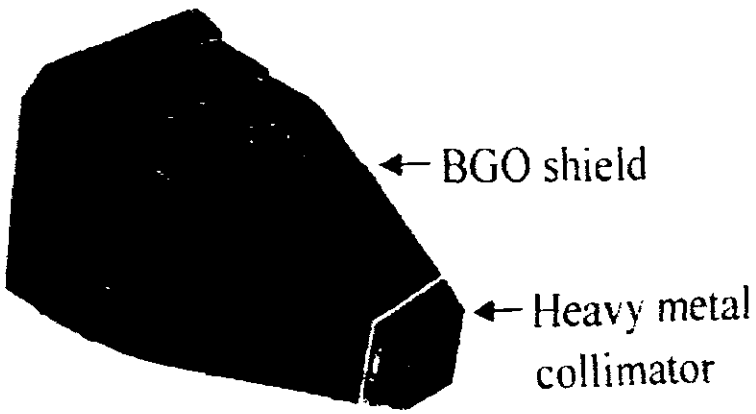

Fig 2.10: shows the BGO Compton suppression shielding

Fig 2.11 shows an example of suppressed and unsuppressed spectra taken with a ^{60}Co source. The normalization of both suppressed and unsuppressed spectra is done such that the number of counts in the photo peaks is constant.

The factor by which the background is reduced is obtained by taking the ratio of unsuppressed to the suppressed spectrum and is called the *Compton Suppression Factor* (CSF). A typical example, of the CFS, measured for the energy range from 300-800 keV, approximately 1.4 [MAB03].

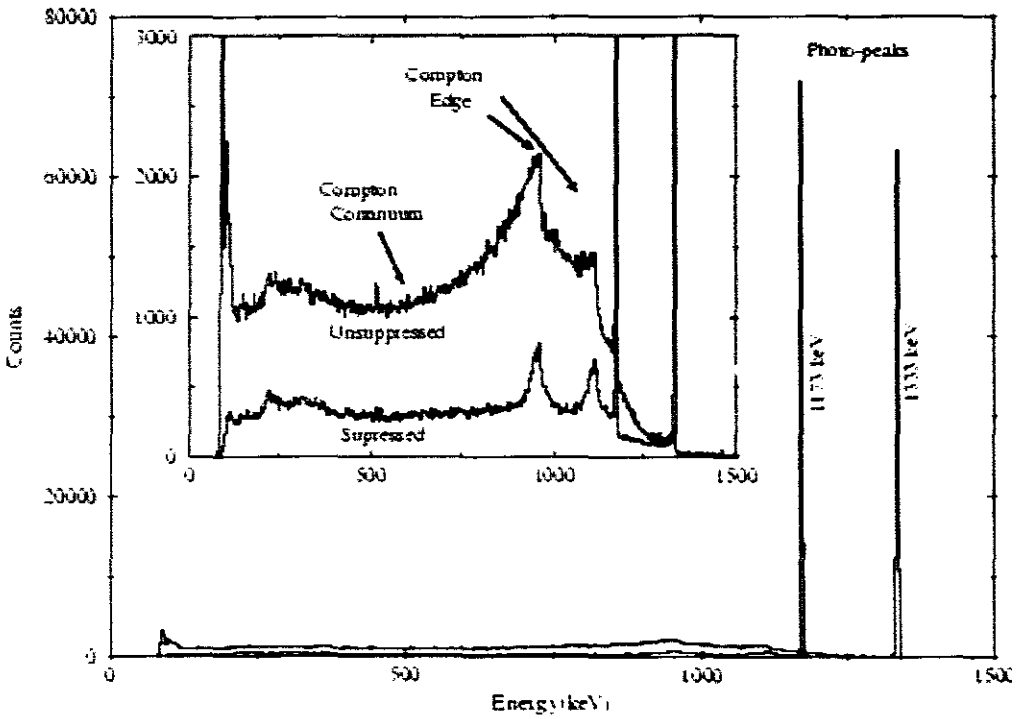

Fig 2.11: *shows the spectra of gamma rays emitted following beta-decay of ^{60}Co to ^{60}Ni. The upper spectrum was obtained with an unsuppressed Ge detector, the lower one with the Ge detector inside an escape suppression shield* [GRE99].

2.3 Rotational model

There are different modes of collective behavior known in nuclei, namely rotation, vibration, deformed nuclei and superdeformation but in this work we are only concerned with rotational states because ^{196}Hg is known to be non-spherical or deformed. The deformed nuclei are known to display rotational bands in their spectra. A rotational band reflects the collective movement of a nucleus which changes the orientation of the system without necessarily changing the shape or intrinsic structure of the nucleus. The kinetic energy associated with the rotation of a rigid body is classically given by:

$$E = \frac{1}{2} J_0 \omega^2 \qquad 2.12$$

If the nucleus is described as a rotating system, the energy due to the rotation is given quantum mechanically as:

$$E_{exc}(I) = \frac{\eta^2}{2J_0} I(I+1) \qquad 2.13$$

In the above equations, J_0 represent the moment of inertia which depends on the shape and internal structure of the nucleus. $E_{exc}(I)$ is the excitation energy of the level with angular momentum I of the rotational band and ω represents angular frequency.

2.4 Rotational bands

2.4.1 Ground-state bands (g.s.b.) of even-even nuclei

The ground state bands of deformed even-even nuclei consist of stretched E2 transitions that are built above the 0^+ ground state. All the nucleons are paired and the nucleus rotates as a whole around the rotational axis, which is perpendicular to the symmetry axis of the nucleus. The spins of the levels are given as: $I^{\pi}=0^+, 2^+, 4^+, 6^+$, etc. and the energies of the levels are given by the equation 2.13 above.

2.4.2 Strongly-coupled bands

Strongly-coupled bands reflect the rotation of nuclei with one or more odd nucleons when the single particle angular momentum $\vec{j}$ is coupled to the collective rotation of the nucleus $\vec{R}$. The projection of $\vec{j}$ on the symmetry axis of the nucleus, K=Ω is a good quantum number as shown in figure 2.12(a). These bands are observed for relatively large nuclear deformation and not very high rotational frequencies. The bands contain stretched M1 and E2 transitions. The angular momenta of the levels are: I=K, K+1, K+2, K+3, etc and the excitation energies are given by:

$$E_{exc} = \frac{\eta^2}{2J_0}[I(I+1) - K^2] \qquad \text{if } K \neq 1/2 \qquad 2.14$$

2.4.3 Decoupled bands

Decoupled bands reflect the rotation of nuclei with one or more odd nucleons, for which the odd particles are decoupled from the nuclear rotation. Their angular momentum j is

aligned along the rotation axis (see figure 2.12 (b)) and their motion is independent of the collective rotation of the nucleus. The bands consist of stretched E2 transitions. The projection of $\boldsymbol{j}$ along the rotational axis, i, (good quantum number) is called alignment. The projection of the total angular momentum $\boldsymbol{I}$ along the rotational axis, $\boldsymbol{I}_x$, is called the aligned angular momentum. The spin and the energies of the levels are given by equation 2.15, respectively:

$$I=i,\ i+2,\ i+4,\ etc \text{ and } E_{exc}(I)=\frac{\eta^2}{2J_0}[(I-i)(I-i+1)] \qquad 2.15$$

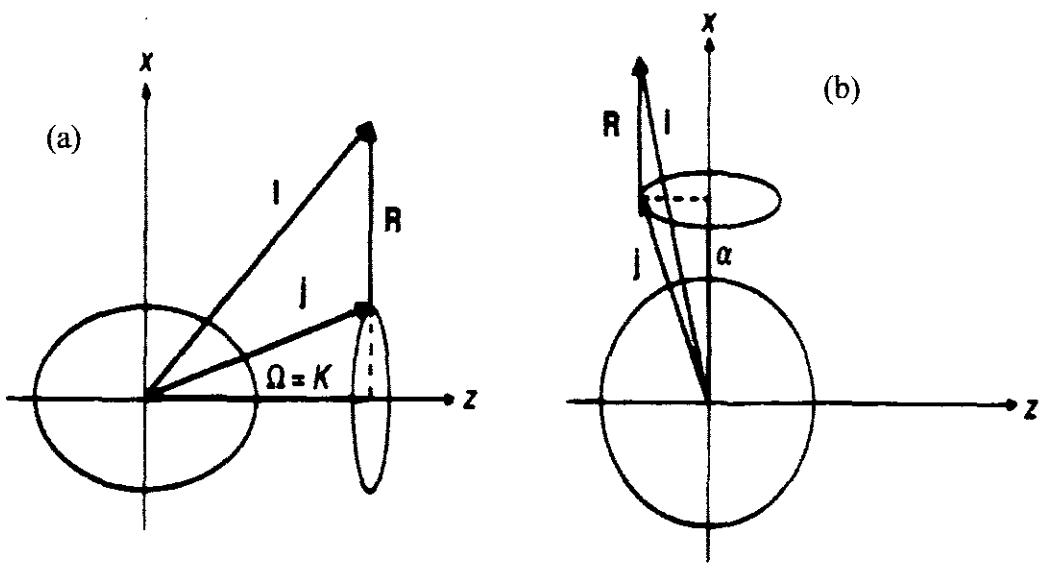

Fig 2.12: illustrates the two extreme coupling schemes; deformation alignment (left figure) and rotation alignment (right figure) from [LIE78].

2.5 Angular distribution

In heavy-ion compound nuclear reactions (HI,xnpα), the multipolarity of the transitions and the spins and parities of the levels are generally determined through the measurement of angular distributions, angular correlations and linear polarizations of γ-rays. The angular distribution of γ-rays $W(\theta)$ is a measurement the intensity as a function of the angle θ with respect to the beam direction or to the nuclear spin axis. The angular distribution function for the case $I_i \rightarrow I_f$ is given by,

$$W(\theta) = \sum_{k even} A_k P_k(\cos\theta) \qquad 2.16$$

where A_k-coefficients are theoretically calculated coefficients which depends on the initial and final nuclear spins, on the multipole order of the radiation and on the mixing ratio δ.

In compound nuclear reactions, it has been established that a wide range of excited states populated in these reactions are well aligned [FER65,YAM67] so that gamma rays exhibit angular distributions depending upon the multipolarities and spin sequences. The simplest technique to analyze the experimental data is to regard the degree of alignment as a parameter that can be determined experimentally or evaluated based on a certain model. The degree of alignment of a state possessing spin I is specified by population parameters $P_m(I)$. The degree of alignment is usually determined through a measurement of $W(\theta)$ for a number of known $\Delta I = 2$ transitions. The attenuation caused by a reduction in the degree of alignment affects only the magnitudes of A_2 and A_4. Angular distribution alone can deduce change in spin ΔI but it can not deduce change in parity $\Delta\pi$.

2.5.1 Angular correlations

Gamma-ray angular correlation measurements are one of the classical γ-spectroscopic tools for determining the spin and parities (I^π) of states and multipole mixing ratios of transitions. The theory of directional correlations of gamma-radiation emitted from oriented states is well developed and discussed by Steffen and Alder [STE75]. In most

applications, the theory of DCO ratio measurements can be simplified with respect to the general directional correlation theory taking into account the experimental conditions [KRÄ89]:

- that unpolarized beams are employed, and
- that the detectors are insensitive to the polarization of the gamma-rays.

The DCO method is similar to the angular distribution method, and is used when the measured angular distribution data points (number of angle) are insufficient for the accurate fitting with an angular distribution function. Angular correlations or **D**irectional **C**orrelations of γ-rays from **O**riented states of nuclei (DCO) measurements involve the determination of the coincidence intensities for two γ-rays which are detected at two different angles i.e. θ_1 and θ_2 with respect to the beam direction. The DCO ratios are defined as $R = \frac{I(\theta_1)}{I(\theta_2)}$. These ratios are insensitive to spin for high spin states but are sensitive to relative spins and multipolarities [SIG01].

Advantages of DCO measurement in comparison with the study of angular distributions are that:

- weak transitions can be studied
- members of multiplets can be analyzed and
- no normalization to the beam charge is necessary.

2.6 The linear polarization of γ-rays

To determine whether the radiation is electric or magnetic in character, additional measurements are necessary since the angular distribution coefficients A_2 and A_4 are the same for E and M radiation. It is however possible to distinguish between electric and magnetic radiation by determining the direction of the electric field **E** with respect to the axis of quantization, since this field will be either parallel or perpendicular to this axis. We thus need to measure the polarization of the γ-radiation. It is known that all polarimeters for linearly polarized gamma radiation rely on the fact that in Compton scattering there is a preferred direction of scattering of the scattered photon relative to

the electric vector of the incident γ-ray photon. This can be seen from the Klein-Nishina cross-section formula [SCH98] given by,

$$\frac{d\sigma^{KN}}{d\Omega}(\theta,\phi)=\frac{r_0^2}{2}\left(\frac{E'}{E}\right)^2\left(\frac{E'}{E}+\frac{E}{E'}-2\sin^2\theta\cos^2\phi\right) \qquad 2.17$$

where r_o is the classical electron radius, $r_o \approx 2.818$ fm, E and E' are the energies of the incoming and the outgoing photon respectively, θ is the angle of the outgoing photon with respect to the incident photon, and ϕ is the angle between the electric vector of the incident γ-ray and the reaction plane containing the incident and scattered photon (see fig 2.13). The equation 2.17 shows that the maximum cross-section of scattering is at $\phi = 90°$.

The degree of polarization at the angle θ to the beam direction is defined as,

$$P(\theta)=\left[\frac{W(\theta,0°)-W(\theta,90°)}{W(\theta,0°)+W(\theta,90°)}\right] \qquad 2.18$$

where $W(\theta,\phi)$ is the probability of the emission of a γ-ray from an aligned state at the angle θ to the alignment axis and with the electric field vector at an angle ϕ to the reaction plane. If the γ-ray is completely polarized in the reaction plane in fig 2.13, then P(θ)=+1 [OLN75]. Experimentally we measure the polarization anisotropy as,

$$S(\theta)=\frac{(N_0-N_{90})}{(N_0+N_{90})} \qquad 2.19$$

where N_0 and N_{90} are the areas under the photopeaks of a given γ-ray measured in two polarimeters with detectors in parallel and perpendicular to the reaction plane, respectively. For the clover detectors in AFRODITE this would correspond to horizontally and vertically scattered γ-rays. P(θ) and S(θ) are related to each other by:

$$P(\theta)=S(\theta)/Q \qquad 2.20$$

where Q is a measure of the sensitivity of a system of finite detectors to linear polarization. Q is related to the asymmetry R, the ratio of the cross section from Compton scattering of the photon into direction parallel and perpendicular to the polarization vector as,

$$Q = \frac{R-1}{R+1}, \tag{2.21}$$

and R is given by

$$R = \frac{\frac{d\sigma}{d\Omega}(parallel)}{\frac{d\sigma}{d\Omega}(perpendicular)} \tag{2.22}$$

Duchêne *et al*, [DUC99] reported values of Q for clover detectors that vary from 0.24 at low energy 280 keV to 0.10 at higher energies (1300 keV).

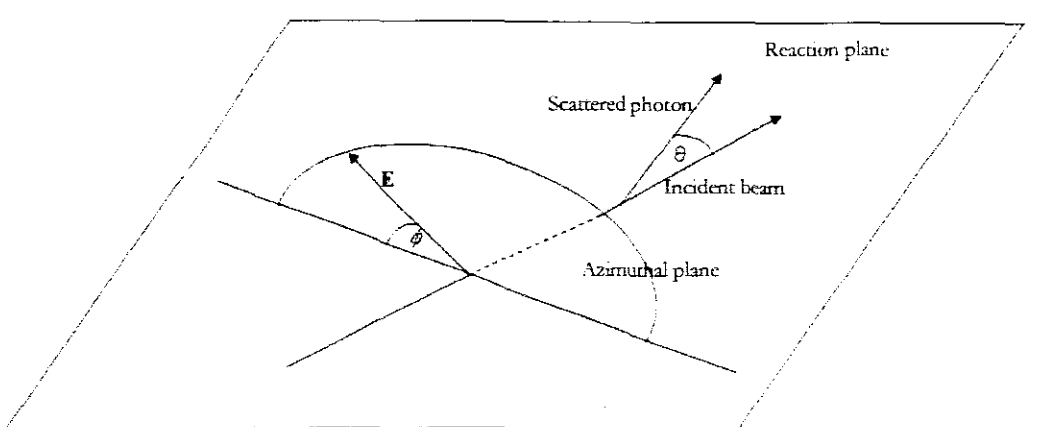

Fig 2.13: illustrate angles and vectors involved in a reaction sensitive to the linear polarization of a γ-ray

2.7 Multipolarity and gamma ray selection rules

The gamma-ray photon energy (E_γ) is equal to the difference or transition energy between the initial and final nuclear states. An excited nucleus may lose its energy by either emission of γ-ray photon or internal conversion. Gamma radiation is the same type of electromagnetic radiation as others, where a change in electric field induces a magnetic field and vise versa. A classical electromagnetic field produced by oscillating charges and current transmits not only energy but also angular momentum. The angular momentum of the photon between initial and final transition states must be conserved following the vector equation 2.22.

$$\mathbf{I}_i = \mathbf{L} + \mathbf{I}_f \qquad 2.22$$

A photon carries away angular momentum of magnitude Lh, where L can have an integer value greater than zero [LIL01]. A γ-ray photon with multipolarity L is either electric (EL) or magnetic (ML), or a mixture of these. Emitting a gamma photon with multipolarity L changes the spin I of the nucleus according to the selection rule, stating that between two nuclear states the largest possible value of L is $I_i + I_f$ and the smallest possible value is $|I_i - I_f|$. This rule is given as,

$$|I_i - I_f| \le L \le I_i + I_f \qquad \text{(no L=0)} \qquad 2.23$$

The change in parity π for EL and ML transitions is governed by:

$$\pi_i \pi_f = (-1)^L \qquad \text{for EL transitions}$$

$$\pi_i \pi_f = (-1)^{L+1} \qquad \text{for ML transitions}$$

index *i* and *f* denote initial and final respectively.

Then,

$\Delta\pi = no$: even electric, odd magnetic

$\Delta\pi = yes$: odd electric, even magnetic.

For radiative transitions, L=0 is not permitted because it will lead to monopole transitions [KRA88].

2.8 Propagation of errors

In experimental work the various quantities which are measured will have errors associated with them. In the measurements of DCO ratios (R_{DCO}) and polarization anisotropy (A_p), we were required to estimate errors associated with this measurements. Since the errors on areas determined from the GF3 program tend to be unrealistically small, we first determine errors at a few energies and extrapolate the errors linearly in energy and then propagate using appropriate mathematical formulas.

In both cases, *i.e.* R_{DCO} and A_p we assumed the measured quantities are independent. In the case of DCO ratios, the combined error is given by,

$$\Delta R_{DCO} = R_{DCO}\sqrt{\left(\frac{\Delta A_{45^\circ}}{A_{45^\circ}}\right)^2 + \left(\frac{\Delta A_{90^\circ}}{A_{90^\circ}}\right)^2} \qquad 2.24$$

In A_p measurements, the number of counts in vertical scattered γ-rays (N_V) is independent of the number of counts in horizontal scattered γ-rays (N_H), and thus the error is given by,

$$\Delta A_p = 2\sqrt{2}\frac{VH}{n^2}\sqrt{\left(\frac{\delta_V}{V}\right)^2 + \left(\frac{\delta_H}{H}\right)^2} \qquad 2.25$$

where n=V+H a total number of counts, in our case V and H stands for vertical and horizontal scattered events respectively.

CHAPTER 3 EXPERIMENTAL DATA ANALYSIS

3.1 Experiment

The data used in this project were obtained from an experiment where high spin states in ^{196}Hg that were populated by the ^{198}Pt(α,6n) reaction at incident beam energy of 65 MeV. The experiment was performed at iThemba LABS with the AFRODITE array, and the beam was supplied by SSC. The target of 200 μg/cm^2 ^{198}Pt was used with an enrichment of 96%. The original purpose of the experiment was to calibrate the AFRODITE array for lifetime measurement with the Recoil Shadow Anisotropy Method (RSAM) [GUE01] making use of the known lifetimes nanosecond isomers in ^{196}Hg. Although this is the same reaction used by Mehta *et al.*[MEH91] as discussed in section 1.5 (Introduction), the present experiment was done with a substantially larger array of gamma detectors allowing the observation of weaker transitions. The data contains both timing and energy information and was recorded on the digital-linear tapes (DLT). In the first part of the experiment ~4 x 10^8 γ-γ coincidence events were recorded with 7 clovers at 90° and 4 LEPS at 45°, and 1 clover and 3 LEPS at 135°. This arrangement was needed for the RSAM calibration and is not ideal for DCO ratio measurements which are essential for spin assignment. A further ~1 x 10^8 coincidence events were recorded with 4 clovers and 3 LEPS at 90°, 4 LEPS at 45° and 3 clovers and 1 LEPS at 135° to assist in the measurements of DCO ratios. The γ-γ coincidence events were sorted into matrix form, after energy calibration and taking into account the Doppler shift effect. The details of electronics used in this experiment and data processing modules are given in ref. [ROU01].

3.2 Data analysis

Since a masters thesis project is strongly limited in time, it is not possible to perform every single step in the data analysis of an experiment performed with such complex detector systems as AFRODITE, therefore, almost all data used in the analysis was already sorted beforehand, into matrices and spectra suitable for further coincidence

analysis. The project concentrated on the determination of spins and parities by measuring the multipolarity of emitted γ-rays using DCO and linear polarization measurements. In addition a γ-γ coincidence analysis was done to confirm the level scheme that was previously obtained from this data set [LAW06].

The event-by-event γ-energies measured with clover detectors were sorted into two-dimensional matrices after energy calibration and Doppler shift correction and correction for drift during runs. From the RadWare software that was developed by David Radford two packages [RAD95] were used in this project.

i. Escalator (ESCL8R) and
ii. GF3

Escalator is important for the energy level scheme construction and gating process with symmetric matrices. The GF3 package is more important for the graphic display and analysis of one dimensional spectra e.g. for peak fitting and area. GF3 is also used for the generation of background-subtraction, gate spectra and total projections from asymmetric matrices e.g. as are used in DCO measurements.

3.2.1 Energy calibration

Radioactive sources used for the energy calibration are europium (^{152}Eu) and barium (^{133}Ba). The ^{152}Eu and ^{133}Ba sources emit gamma-rays in the range of 45 – 1408 keV and 30 – 400 keV, including their X-rays, respectively. Energy calibration data were recorded before and after every weekend during the experiment. The peak centroids for all the γ peaks in the Eu and Ba spectra were determined by a peak fitting program and energy calibration coefficients were determined by fitting equations i.e. linear, quadratic. In this experiment a linear energy calibration was used to calibrate the energy vs channel number data.

3.2.2 Doppler shift

If a γ-ray source moves at velocity v, the detected gamma-rays undergo Doppler shift. The relationship between the detected and emitted gamma-rays energy is given by:

$$E_\gamma = \frac{E_\gamma^0\sqrt{1-\beta}}{1-\beta\cos\theta} \sim E_\gamma^0(1+\beta\cos\theta) \qquad 3.1$$

where E_γ is the energy of the detected γ-ray at an angle θ, E_γ^0 is the emitted gamma-ray energy and β is the ratio of velocity v to the speed of light c *i.e.* $\beta=v/c$.

Equation 3.1 shows that the maximum Doppler shifts are observed along the beam direction *i.e.* at =0°and 180°, while the minimum is at angle θ=90°.

Taking into account the solid angle subtended by the detector, the energy difference between the energy entering the detector at angle θ-$d\theta$ and angle θ+$d\theta$ is given by:

$$\Delta E = \left|E_\gamma(\theta+d\theta) - E_\gamma(\theta-d\theta)\right| \qquad 3.2$$

then

$$\Delta E = 2E_\gamma^0 \sin\theta \sin d\theta \qquad 3.3$$

Equation 3.3 shows that the Doppler Effect broadening is maximum at θ= 90° and zero at θ= 0°. The small size of each detector element obtained through segmentation of the crystals, reduce the uncertainty in the angle θ and thus the energy E_γ can be better calculated.

3.3 Gamma-gamma matrices

Complex nuclear level schemes are deduced mainly from the analysis of γ-γ coincidence matrices. The information obtained from these matrices is qualitative and quantitative. For instance, to determine which γ-rays are in coincidence is qualitative information. To determine how much of the feeding or decay of a given level can be ascribed to different transitions, is quantitative information [VAN89].

If two gamma-rays are detected in coincident with energies $E_{\gamma 1}$ and $E_{\gamma 2}$ the pair ($E_{\gamma 1}$,$E_{\gamma 2}$), is referred to as a γ-γ coincidence. Those γ-γ coincidence events are stored in a two-dimensional energy histogram (usually referred to as the symmetrized matrix with 4096 x

4096 channels). The energy of one photon is placed on one axis of the matrix, and the energy of the other coincident photon on the other axis. The matrix is normally symmetrized by increasing the matrix with ($E_{\gamma 1}$,$E_{\gamma 2}$), ($E_{\gamma 2}$,$E_{\gamma 1}$) for each coincidence. The total projection of the matrix is obtained by projection of all counts onto one energy axis, which results in a one-dimensional γ-ray spectrum. Selecting a narrow region around a photo-peak on one of the two energy axes and projecting onto the other axis, all the γ-ray energies in coincidence with that peak to obtain a coincidence γ-ray spectrum is referred to as gating. In this work all the spectra were background-subtracted during the analysis.

3.4 The linear polarization analysis

Linear polarization measurements can be performed with gamma ray arrays containing clover detectors. The clover detectors consist of four different HPGe crystals embedded in the same cryostat (see fig 2.9), allowing the observation of Compton scattered events between different elements in the clover detector. The experimental data was sorted in such a way that the events corresponding to the scattering parallel to the plane defined by the beam direction and the γ-ray direction are sorted in a spectrum called "horizontal" and those corresponding to the scattering perpendicular to this plane are sorted in a spectrum called "vertical". In general, one measures the polarization anisotropy (A_p) as:

$$A_p = \frac{N_V - \varepsilon N_H}{N_V + \varepsilon N_H}, \qquad 3.4$$

where N_V and N_H are the counts measured, for the analyzed γ-line in the vertical and horizontal spectra respectively and ε is the relative efficiency of the detector crystal. For this work, the relative detector efficiency ε was measured using a europium source and found to be 1.0. The polarization anisotropy has positive sign for stretched electric transitions and negative sign for stretched magnetic transitions and it is opposite for unstretched transitions. A spectrum constructed as the difference between the spectra of vertical and horizontal double-hit events N_V-εN_H is shown in figure 3.1. The peaks with positive number of counts represent stretched electric transitions, while these with

negative number of counts show stretched magnetic transitions. As discussed above, clover detectors have been used to perform the linear polarization measurements but their sensitivity to the polarization of γ transitions will be reduced due to the close packing of the crystals. The polarization anisotropy is proportional to the linear polarization P, and the quality factor Q (equation 2.20). From the results of Duchêne *et al.*[DUC99] we can expect the absolute value of the anisotropy to be ~0.05 - 0.15. The linear polarization is proportional to polarization anisotropy.

In this project we were unable to get the similar spectra as in fig 3.1 for the determination of the multipolarity. The reason being that, (i) the peaks in vertical and horizontal spectra were superimposed on the large background, (ii) low probability of the double-hit (two crystals hit in coincidence) events in the clover detectors results in low statistics obtained in the spectra, and (iii) Since a thin target was used, peaks are Doppler broadened as a result of recoil into vacuum. The Doppler broadening is however not the same for vertical and horizontal scattered events resulting in differences in peak shapes. Subtraction of spectra therefore gave large positive or negative spikes as a result of the differences in peak shape. Therefore in order to measure polarization anisotropy, spectra were generated from vertical and horizontal total projection spectra with some gate set on them.

The polarization anisotropy was therefore obtained from peak areas using equation 3.4. Vertical and horizontal spectra for transition of interest, after gating on suitable coincident transitions, were obtained by sorting the energy calibrated event data. Background subtracted peak areas were obtained using GF3 and errors were estimated by combining the statistical errors on the total area and on the area of the background under the peak.

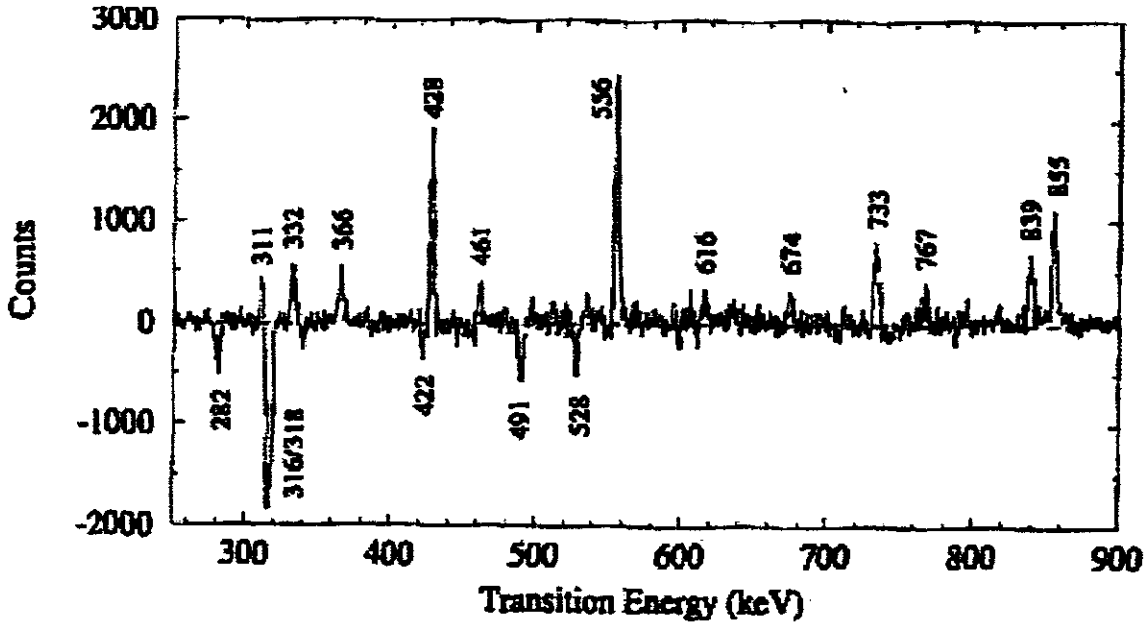

Fig 3.1: shows polarization spectrum N_V-εN_H obtained with Eurogam-II. N_V and N_H correspond to measured count number of vertical and horizontal double-hit events [GUE99].

3.5 DCO ratio measurements

In the AFRODITE array, the Ge detectors are arranged to be at angles 45, 90, 135 degrees with respect to the beam direction. Due to symmetry around 90° data at 45°and 135° can be combine and is referred to as 45° data. DCO ratio measurement with the AFRODITE array are normally done by sorting γ-γ coincidence data into a symmetric 45°-45° matrices and asymmetric 90°-45° matrices. DCO ratios can then be obtained as the ratio of the areas of peaks in projections onto the 45° and 90° axes respectively [ROU01,MAB03]. Alternatively, it is also possible to construct two asymmetric matrices of 45° vs "all" and 90° vs "all" where "all" refers to γ-rays detected at any angle (45°, 90°, or 135°). The DCO ratios are determined as above from projections onto the 45° and 90° axes. It has been shown that for the AFRODITE geometry these two methods are equally sensitive at discriminating between dipole and quadrupole transitions [MAS05].

In this analysis the latter method was used since it gives more counts in the projected spectra.

The DCO analysis could only be done on data from the second part of the experiment where detectors were placed at 45°, 90° and 135° giving only ~10^8 events, thus the improvement in statistical accuracy was needed. Gates on transitions close to the transition of interest are placed on the "all" axis for both matrices to get 45° and 90° spectra respectively (see fig 3.2). Both the 45° and 90° spectra were background subtracted by putting a gate on "clean" background regions near the gating transition in both matrices, to form the background spectra.

After normalization for the width of the gates the 45° background spectra were subtracted from the 45° spectra and the same was done for 90°. The areas of peaks in the final background subtracted spectra were obtained by fitting in GF3 and DCO ratios (R_{DCO}) were then calculated from the peak areas for 45° ($A_\gamma 45°$) and 90° ($A_\gamma 90°$) using equation 3.5.

$$R_{DCO} = \frac{A_\gamma(45°)}{A_\gamma(90°)} \qquad 3.5$$

The importance of background subtraction is to reduce the amount of contamination from other Hg isotope nuclei. Where possible DCO ratios for a single transition were obtained from different gates in order to check the consistency of the measurement and to ensure that contamination is avoided.

The R_{DCO} ratios for the previously known dipole and quadrupole transitions for ^{196}Hg were determined and for stretched dipole ($\Delta I=1$) and stretched quadrupole ($\Delta I=2$) transitions, average R_{DCO} were 0.55±0.10 and 0.87±0.13 respectively.

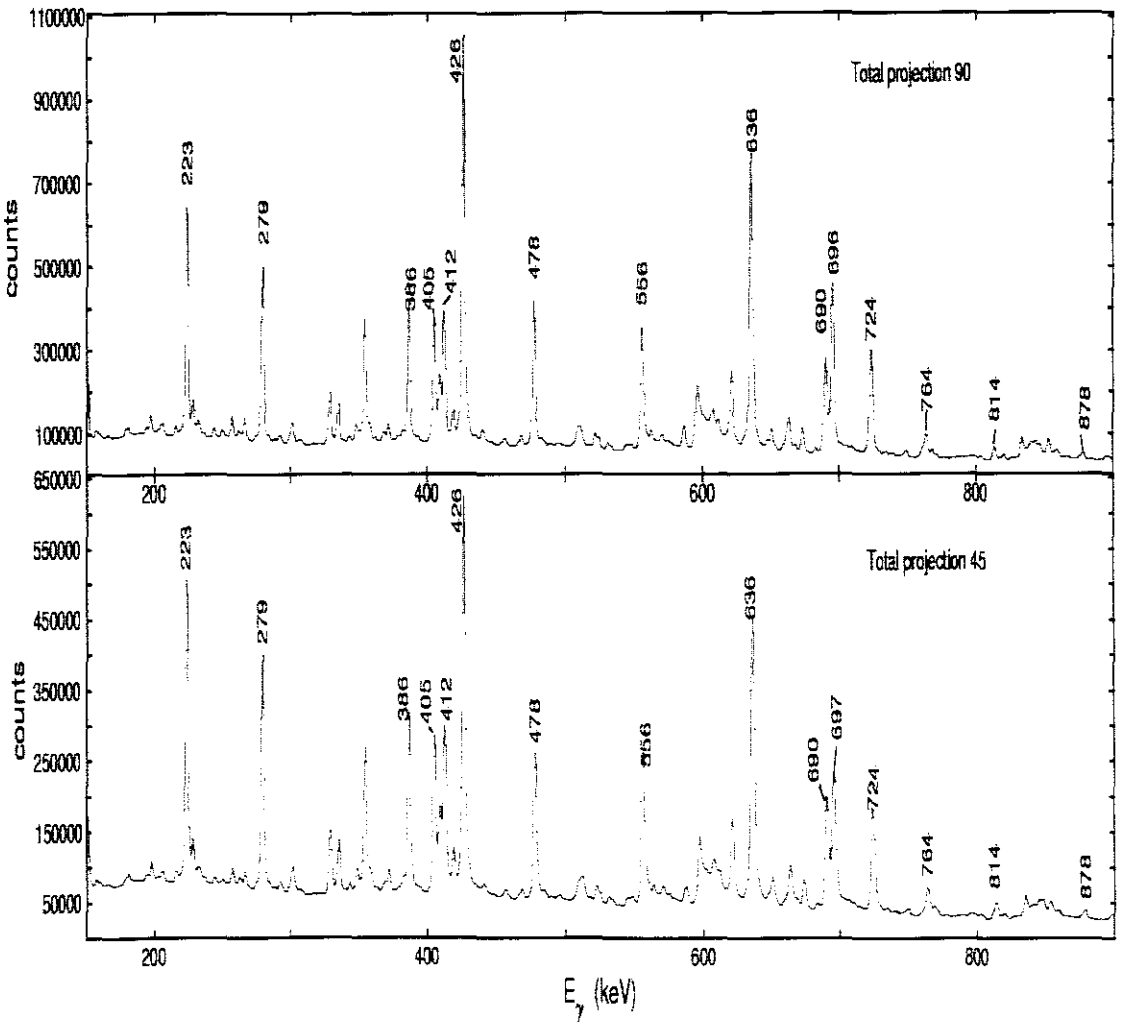

Fig 3.2: shows the total projection spectra for both 45 and 90 degrees

CHAPTER 4 EXPERIMENTAL RESULTS AND DISCUSSION

4.1 Experimental Results

This chapter presents the experimental results for both DCO ratio and polarization anisotropy A_p measurements with the uncertainty associated with them.

4.1.1 The of level scheme of ^{196}Hg

Before the start of this project the γ-γ coincidence data obtained in the experiment described in section 3.1 were used to extend the level scheme of ^{196}Hg [LAW06]. The previously known level scheme [MEH91] is shown in figure 4.8, while the extended level scheme obtained from the present data is shown in figure 4.11 where spin and parity assignments of new levels or of cases where spins and parities where previously unknown are based on this study, as described in section 3.1.2 and 3.1.3.

Although the construction of the energy level scheme was outside the scope of this work, γ-γ coincidence relations were extensively studied to confirm the energy levels and γ-decay paths given in figure 4.11, and are therefore briefly described. The level scheme was investigated using the data analyzing program, ESCL8R [RAD98] to study coincidence relationships from a γ-γ matrix containing data from clover detectors only. A total projection spectrum obtained in the matrix after background subtraction is shown in fig 4.9.

As an example spectra obtained after gating on 426, 223, 556, and 636 keV lines are given in fig 4.10. This figure shows newly observed transitions with energies 1147 keV, 1190 keV, and 1331.2 keV. It can be seen that the 1331.2 keV γ is in coincidence with 426 keV, 223 keV, and 556 keV transitions but not with the 635 keV transition. This confirms the placement of the 1331.2 keV transition between the 5 and the 2^+ levels. From this and other coincidence relations the 1147 keV transition is shown to connect

the bottom of band b with the negative parity band (at the 17^- level) while the 1190 keV transition is situated above the 16^+ level.

In other cases there were some difficulties in placing new transitions due to multiplets (transitions with close energy) e.g. 301.7/300.5 keV, 223/228 keV, 256.5/256.4 keV, 663.9/665 keV γ-ray transitions. Also in many spectra a gated on ^{196}Hg transitions, we observed contaminant peaks mostly from other Hg isotope e.g $^{194, 195, 197}$Hg.

The negative parity band (ABCE in fig 4.8) could not be extended beyond the 23^- level and only one additional level could be added to the positive parity band (22^+ level at 6108 keV). The dipole band observed by Cederwall *et al.*[CED93] was confirmed and it was confirmed that a 1406 keV transition connects this band to the negative parity band, probably above the 21^- level, but the exact placement could not be firmly established, and other decay paths also exist. The structure at 5350 keV observed by Mehta *et al.*[MEH91] is confirmed and extended to both higher- and lower spins. In addition a number of other transitions are observed and placed in the level scheme, although none of these structures could be extended beyond two or three transitions.

4.1.2 Polarization results

The assignment of whether the transition is electric or magnetic in character is supported by linear polarization measurements performed using the clover detectors at 90° to the beam direction as polarimeters. As discussed in the previous chapter (section 3.4), we were required to re-run data tape with gates set on 'clean' peaks (e.g. 426-, 636-, 556-, 386-keV, etc) to obtain spectra shown in fig(s) 4.1 and 4.2 for both vertical and horizontal spectra. To determine peak areas the fitting was done "by hand" using GF3.

The results for polarization measurements are presented in Table 4-1. The negative values of A_p show transitions that are most likely stretched magnetic while the positive value probably represent stretched electric transitions. The signs are reversed for unstretched transitions. The polarization measurements presented in Table 4-1 are for

new transitions or for cases where the parity of the initial state was not known except for the 223 keV transition. We were able to determine the characters (electric or magnetic) of member of doublets e.g. 256.4/256.5 keV (both are magnetic) and 300.5/301.7 keV (both are electric) by selecting appropriate gates. The values of uncertainties given in Table 4-1 were determined as described in section 3.4 for a number of peaks with different intensities and interpolated for the other peaks. The values of the measured polarization anisotropies are generally within the expected range of 0.04 – 0.15 if the uncertainties are taken into account, with the possible exception of the 256.4 and 256.5 keV transitions. These however are fairly weak transitions.

*All the multipolarity assignments can be reasonably accommodated in the level scheme except for the 489 keV transition between the 10^- level at 2554.0 keV and the 9^- level. The spin and parity of the 9^- level is well established while that of the 10^- level is fixed by the M1 character of the 256.5 keV transition and the L=2 nature of the 456.0 keV transition, known from previous work [MEH91] and confirmed by this study. It is thus likely that the 489 keV transition is a M1/E2 with a relatively large mixing ratio causing the polarization anisotropy to be positive.

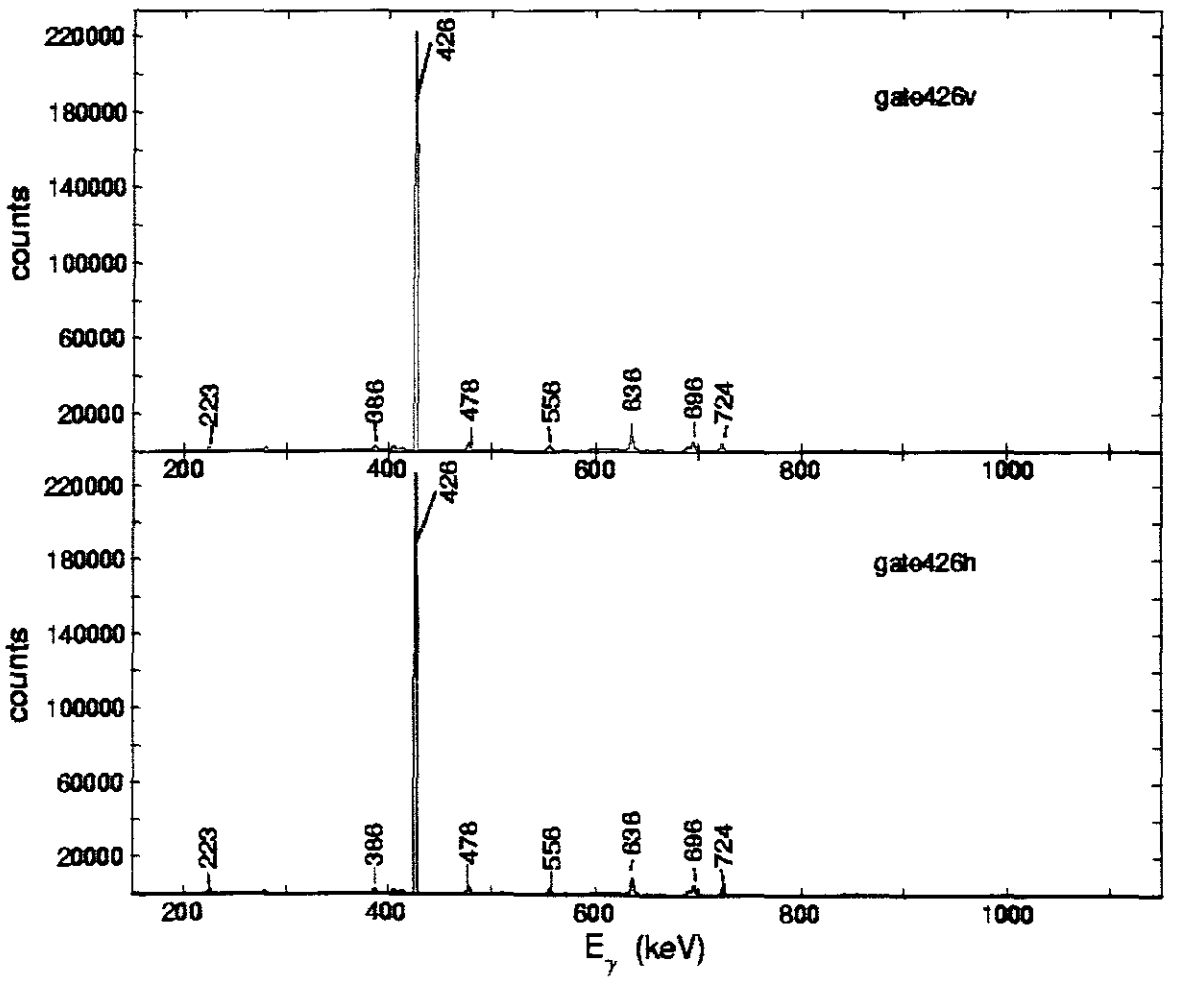

Fig 4.1: shows the example of the gate426 spectra for the polarization measurement. The top (bottom) panel is for vertical (horizontal).

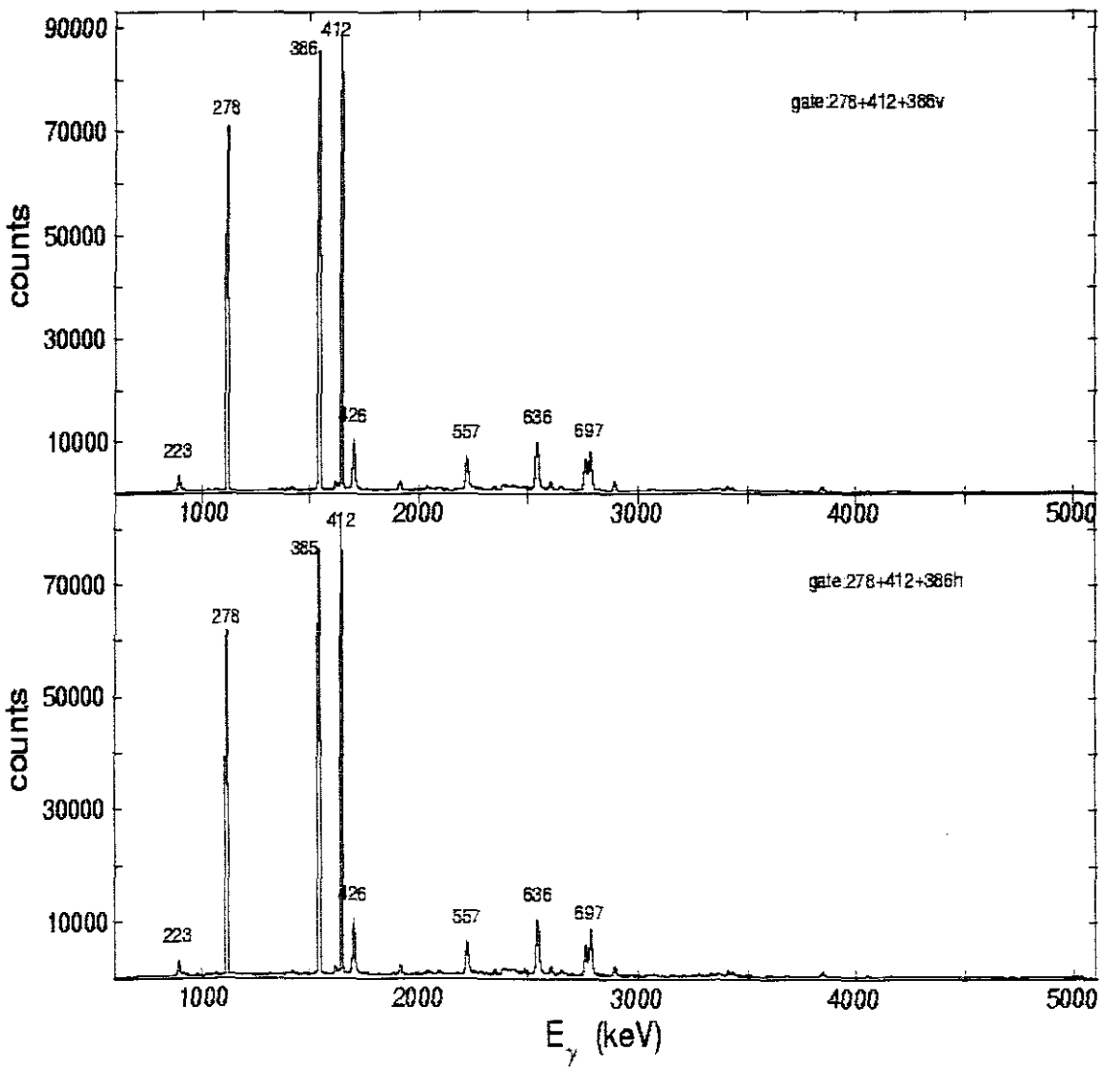

Fig 4.2: shows the example of the summed spectra for the polarization measurement. The top (bottom) panel is for vertical (horizontal).

Table 4-1: shows the measured polarization of gamma-rays values where a value of ε=1.0.

E_γ(keV)	Nv	Nh	Ap	$I_f^\pi \rightarrow I_i^\pi$	E_{exc}(keV)	Multipolarity
223.0	18728	14931	0.11 ± 0.04	$9^- \rightarrow 7^-$	2064.7	E)[b]
243.0	9216	11320	-0.10 ± 0.05	$22^+ \rightarrow 21^+$	5615.9	M
256.5	1071	1720	-0.23 ± 0.06	$8^- \rightarrow 7^-$	2098.0	M
256.4	334	521	-0.22 ± 0.07	$25^+ \rightarrow 24^+$	6960.9	M)[b]
265.9	2081	2674	-0.12 ± 0.05	$21^+ \rightarrow 20^+$	5616.9	M
300.5	1165	976	0.09 ± 0.06	$9^- \rightarrow 7^-$	2359.4	E)[b]
301.7	760	600	0.12 ± 0.07	$7^- \rightarrow 5^-$	2058.9	E
381.3	337	307	0.05 ± 0.03	$13^- \rightarrow 11^-$	3311.2	E
489.0	1200	945	0.12 ± 0.07	$10^- \rightarrow 9^-$	2554.0	E)*
570.5	1557	1336	0.08 ± 0.04	$11^- \rightarrow 9^-$	2929.9	E
575.5	4575	3919	0.08 ± 0.05	$17^- \rightarrow 15^-$	4367.2	E
647.3	530	382	0.16 ± 0.07	$22^+ \rightarrow 20^+$	5847.0	E)[b]
653.0	549	452	0.10 ± 0.07	$24^+ \rightarrow 22^+$	6500.0	E)[b]
665.3	1980	1512	0.13 ± 0.06	$14^- \rightarrow 12^-$	3902.3	E
760.9	2112	1681	0.11 ± 0.05	$13^- \rightarrow 12^+$	3200.0	E
785.0	1141	1026	0.05 ± 0.03	$(15^-) \rightarrow 13^-$	3985.0	E
821.1	2789	2389	0.08 ± 0.05	$22^+ \rightarrow 21^-$	5859.9	E
840.9	3601	2970	0.10 ± 0.05	$(17^-) \rightarrow 15^-$	4632.6	E
907.8	156	132	0.08 ± 0.03	$19^- \rightarrow 17^-$	5275.0	E
920.0	1390	1127	0.10 ± 0.06	$23^- \rightarrow 21^-$	5958.8	E)[b]
948.0	1702	1531	0.05 ± 0.03	$15^- \rightarrow 14^+$	3791.7	E
962.7	6774	5580	0.10 ± 0.05	$20^+ \rightarrow 19^-$	5351.0	E
970.9	776	650	0.09 ± 0.06	$19^- \rightarrow 17^-$	5338.1	E)[c]
1146.7	1401	1132	0.11 ± 0.06	$18^+ \rightarrow 17^-$	5123.0	E
1190.0	2529	2323	0.04 ± 0.02	$18^+ \rightarrow 16^+$	4697.6	E
1331.2	1731	1213	0.18 ± 0.05	$5^- \rightarrow 2^+$	1757.2	E

)[b] previously known multipolarity.
)* see text

4.1.3 DCO ratios results

The GF3 program was used to analyze both the 45° and 90° spectra to determine the directional correlations ratio of oriented states. From the total projection spectra in fig 3.2 we were able to generate several spectra by setting gates on 'clean' peaks e.g. 426 keV, 223 keV, 556 keV, etc. To determine DCO ratios for some weak transitions we were required to sum a number of spectra to increase the statistics. To determine the R_{DCO} for the 1331.2 keV transition, 426 keV, 223 keV, and 556 keV spectra were summed to give the spectrum shown in fig 4.3. The figure 4.4 shows the expanded part of fig 4.3 to properly analyze peak 1331.2 keV. It was notable that gating on 426 keV transition (as shown in fig 4.5) is more or less the same as a total projection.

Table 4.2 show the DCO ratios obtained for different γ transitions. In many cases, the average DCO ratio, averaged over several gates, was used. The values in parentheses represent the errors as explained in section 3.5. One can also note that in transitions 426, 636, 724, 477 keV, we expected the R_{DCO} value to be ~0.87 since they are well established as stretched quadrupole transitions. However the results show that, they are consistently ~0.71. This may be due to the fact they are all below the two isomeric states [PET68][PRO74] with lifetimes of 4.9 and 3.5 ns. A smaller value of the DCO ratio may be due to loss of alignment. However this effect was not observed by Mehta *et al.* [MEH91].

In this experiment a thin target was used thus reaction products recoil into vacuum. For transitions below the isomer, a significant fraction of the γ-decay will take place at some distance from the target centre. This could cause a shadow effect (as is used in the Recoil Shadow Anisotropy Method for determining lifetimes) but the influence among the detectors differs from each and every angle (45°, 90° or 135°). Such an explanation would be consistent with the fact that this reduction in DCO ratio was not observed by Mehta *et al*, where a thick target was used. Figure 4.6 shows the relationship between γ-ray energy and R_{DCO}. The measured averaged R_{DCO} ratios for known dipole and

quadrupole transitions are shown with dash lines. Figure 4.7 illustrates the measured values of R_{DCO} for previously determined [MEH91] pure stretched quadrupole transitions below the 12^+ and 10^+ isomeric states.

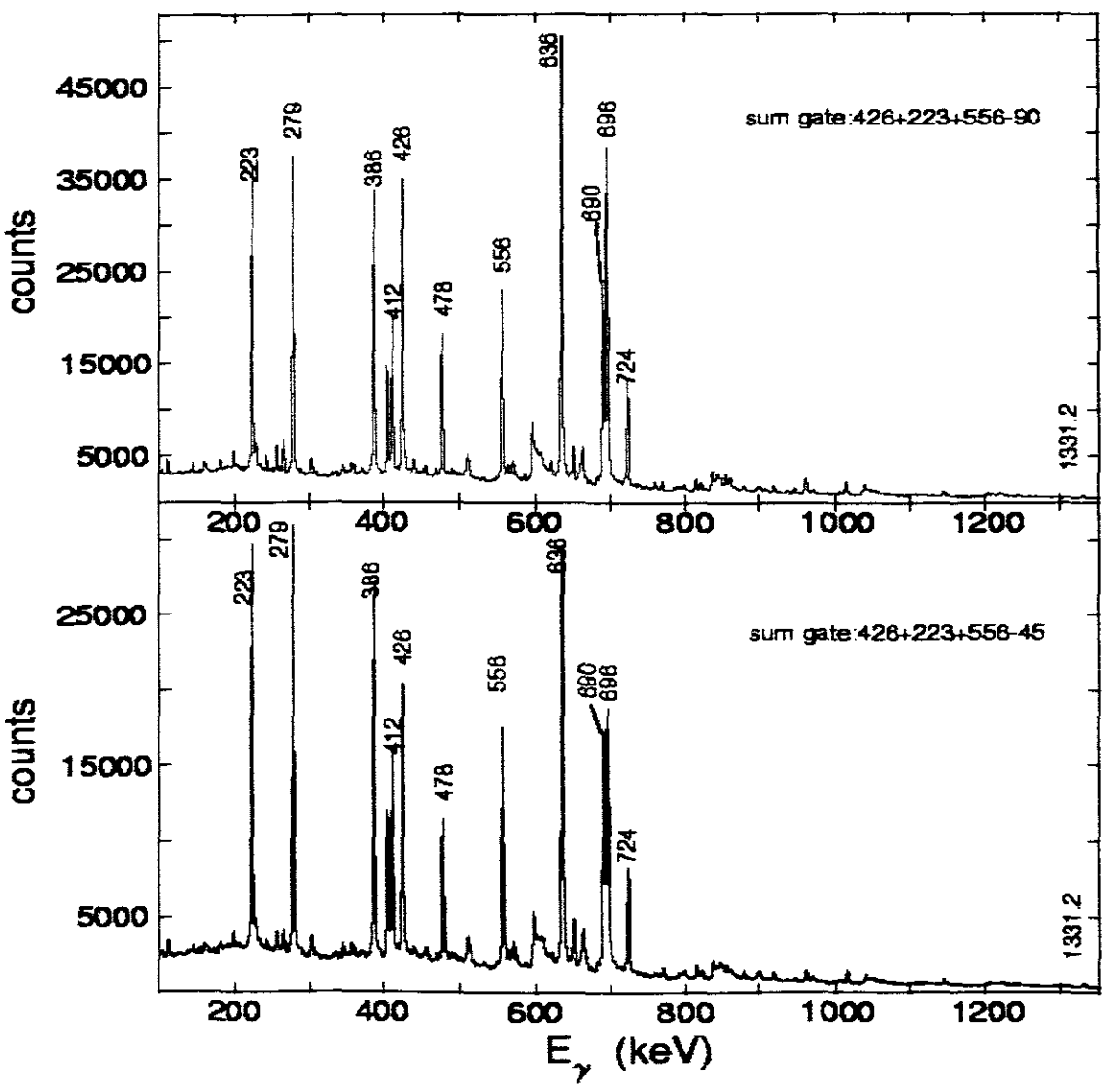

Fig 4.3: shows the sum gated spectra, the upper panel represents 90°while the bottom panel represents 45°.

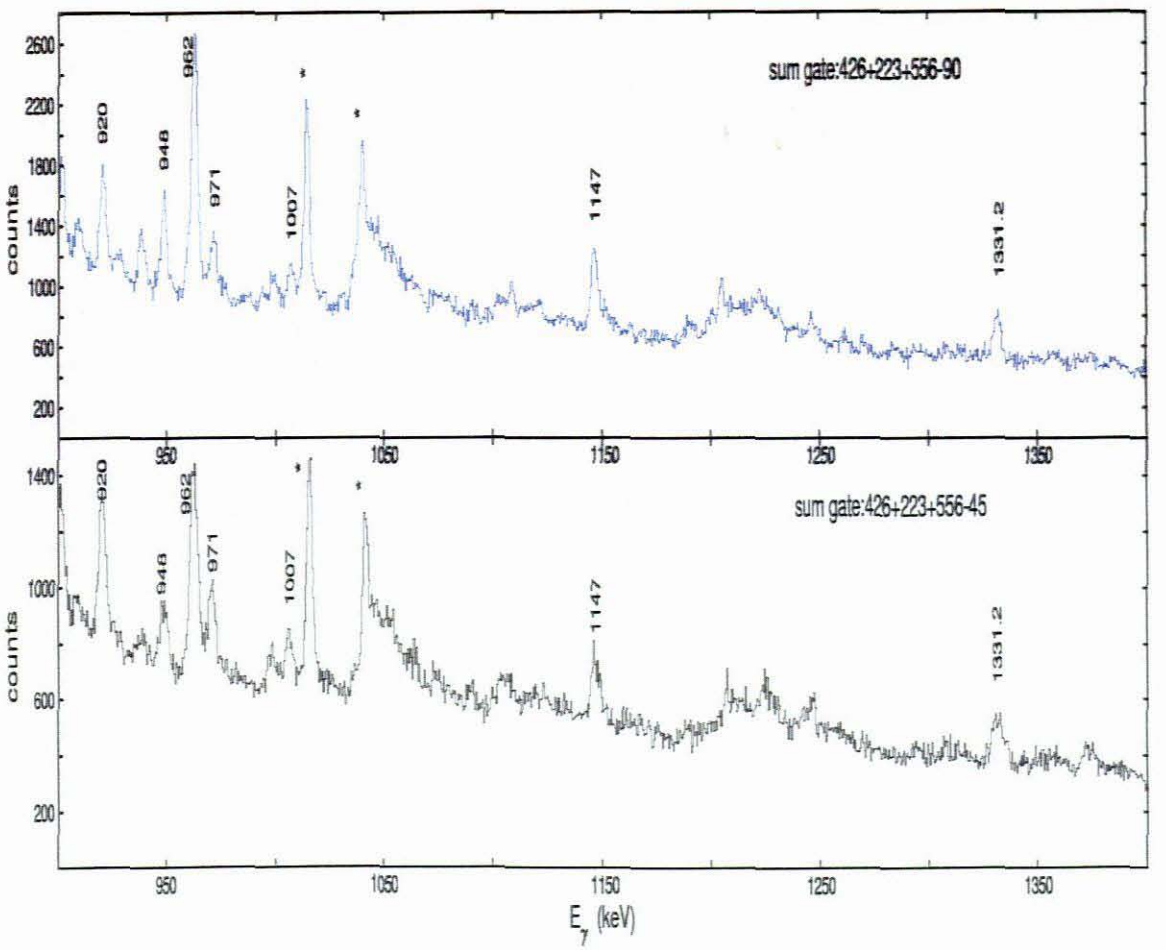

Fig 4.4: shows the expanded part of fig 4.3 for the proper analyses of 1331.2 keV transition. The peaks that are marked with the stars do not belong to ^{196}Hg.

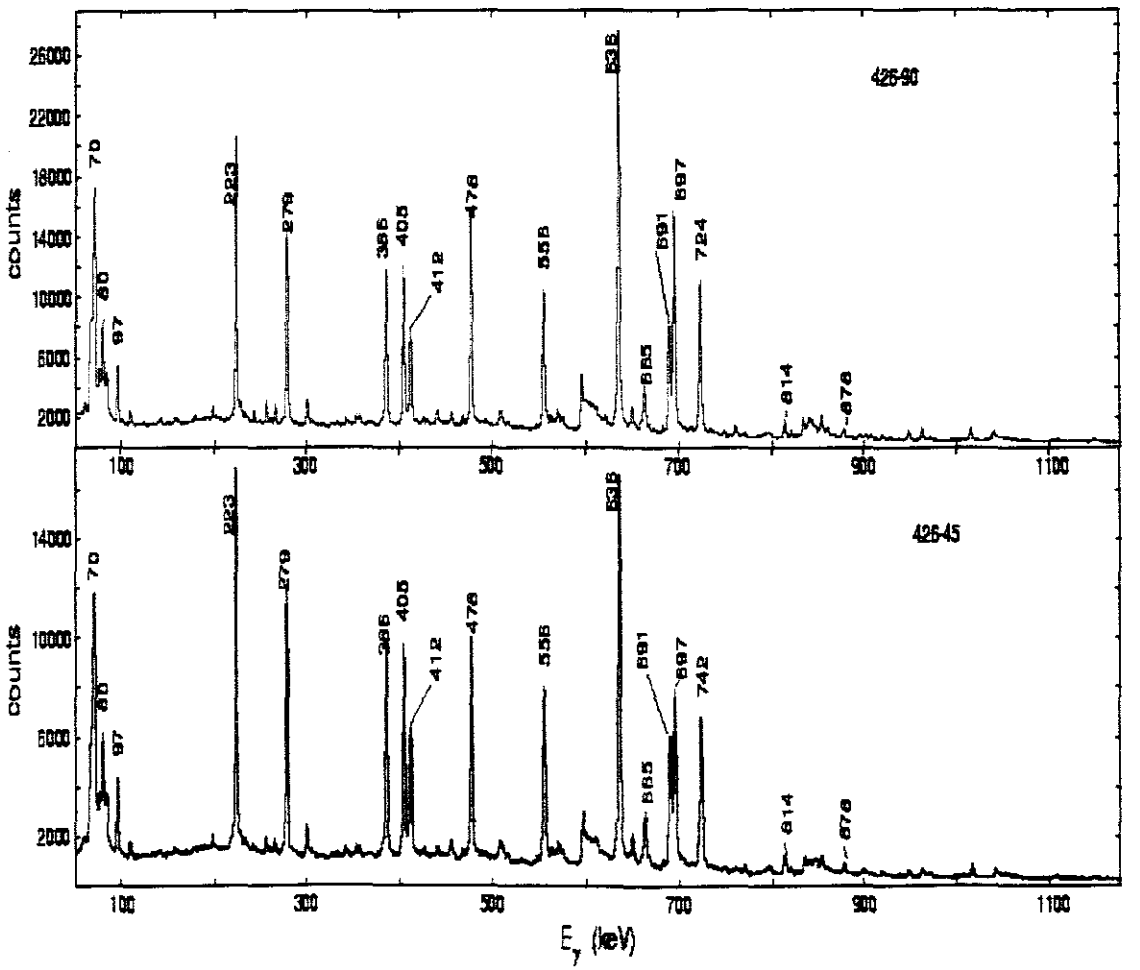

Fig 4.5: shows the number of peaks that are present for DCO measurements when gated on 426 keV transition. Top panel for 90° and bottom panel for 45° spectra respectively.

Table 4-2: represent the measured A(45°/90°) and the calculated values of R_{DCO}

E(keV)	Gated on	$A_\gamma(45°)$	$A_\gamma(90°)$	R_{DCO}[√]		$I_f^\pi \rightarrow I_i^\pi$	ΔI	E_{exc} (keV)
223	386	57515	66079	0.87(4)	0.85(4)	$9^- \rightarrow 7^-$	2	2064.0
	278	53875	64748	0.83(4)				
	556	52455	61320	0.86(4)				
243	386	1028	1629	0.63(21)	0.52(4)	$22^+ \rightarrow 21^+$	1	5859.9
	278	1896	3995	0.47(9)				
	556	1290	2772	0.47(11)				
256.4	386	1213	2366	0.51(13)	0.56(11)	$(25^+) \rightarrow (24^+)$	1	6960.9
	278	2276	4530	0.50(8)				
	556	2026	3108	0.65(12)				
256.5	456	1294	2579	0.50(12)	0.51(11)	$8^- \rightarrow 7^-$	1	2098.0
	665 + 456	2022	3849	0.53(9)				
265.9	386	2337	4597	0.51(7)	0.48(7)	$21^+ \rightarrow 20^+$	1	5616.9
	278	3854	8421	0.46(6)				
300.5	570	2261	2673	0.85(16)		$9^- \rightarrow 7^-$	2	2359.4
301.7	683+456	2601	3010	0.86(15)		$7^- \rightarrow 5^-$	2	2058.9
381.0)[d]	570	891	1022	0.87(20)		$13^- \rightarrow 11^-$	2	3311.2
386.3	570	5174	5958	0.87(7)	0.87(7)	$15^- \rightarrow 13^-$	2	3697.5
	426 + 278	79386	90414	0.88(7)				

404.6	635.6	34566	38402	0.90(6)	0.91(5)	$14^+ \rightarrow 12^+$	2	2843.7
	724	28219	30908	0.91(7)				
	724 + 635.6	63774	69606	0.92(4)				
412.0	386	23100	25759	0.90(9)	0.90(7)	$19^- \rightarrow 17^-$	2	4388.3
	635.6	29947	34282	0.87(6)				
	724	5847	6117	0.96(12)				
	724 + 635.6	37248	41734	0.89(5)				
426	635.6	96096	141198	0.68(2)	0.69(3)	$2^+ \rightarrow 0^+$	2	426.0
	724	39562	55238	0.72(4)				
	724 + 635.6	136935	198817	0.69(2)				
456	301.7	1377	1691	0.81	0.83	$10^- \rightarrow 8^-$	2	2554.0
	256 + 683	2447	2912	0.84				
468.7	664	1674	3200	0.52(12)	0.54(12)	$17^- \rightarrow 16^+$	1	3976.3
	(644 + 426 + 724)	4269	7535	0.57(7)				
477.6	426	50775	70885	0.72(3)	0.72(3)	$8^+ \rightarrow 6^+$	2	2263.0
	635.6	38588	54084	0.71(4)				
	724	33127	45737	0.72(4)				
	(426 + 724 + 635.6)	122438	170579	0.72(2)				
489	223	1685	2099	0.80(19)		$10^- \rightarrow 9^-$	2)*	2554.0

556.1	456 + 426 426 223 386	48837 45588 53852 39993	56606 49880 62204 45636	0.86(4) 0.91(5) 0.87(4) 0.88(5)	0.88(5)	$11^- \rightarrow 9^-$	2	2620.8
570.5	426	5747	6762	0.85(10)		$11^- \rightarrow 9^-$	2	2929.9
575.5	948 426	1300 3282	1597 3479	0.81(20) 0.94(15)	0.88(19)	$17^- \rightarrow 15^-$	2	4367.2
635.5	426 477	103106 42699	143583 59595	0.72(2) 0.72(3)	0.72(3)	$4^+ \rightarrow 2^+$	2	1061.5
647.3)[d]	878.2	1938	2131	0.91(19)		$22^+ \rightarrow 20^+$	2	5847.0
653)[d]	878.2	831	963	0.86(20)		$24^+ \rightarrow 22^+$	2	6500.0
663.8	426	13861	16238	0.85(9)		$16^+ \rightarrow 14^+$	2	3507.6
665.3)[d]	301.7 301.7 + 456	2581 5829	3260 6915	0.79(13) 0.84(10)	0.79(12)	$14^- \rightarrow 12^-$	2	3902.3

683.0	301.7	722	779	0.93(20)	0.87(20)	$12^- \rightarrow 10^-$	2	3237.0
	456	1099	1357	0.81(19)				
690.4	386	35762	43211	0.83(5)	0.82(15)	$13^- \rightarrow 11^-$	2	3311.2
	278	30700	37516	0.82(5)				
695.7	386	30323	57775	0.52(3)	0.52(15)	$5^- \rightarrow 4^+$	1	1757.2
	278	26251	51143	0.51(4)				
	301.7	8358	15676	0.53(6)				
741)[d]	(426 + 724 + 636)	438	870	0.50(20)		$14^{(-)} \rightarrow 13^-$	2	3941.0
760.9)[d]	(426 + 724 + 636)	5532	11649	0.47(11)		$13^- \rightarrow 12^+$	1	3200.0
794.6)[d]	(724 + 426 + 948)	3063	4635	0.66(9)	0.71(9)	$(18^+) \rightarrow (17^-)$	1	5427.2
	(426 + 724 + 636)	4962	6476	0.77(10)				
799.0)[d]	570 + 426	1729	2129	081(18)	0.94(20)	$15^{(+)} \rightarrow 13^-$	2	4110.2
	556 + 223	2151	2267	095(19)				
	(426 + 223 + 556)	5492	5182	1.06(14)				
	556 + 426	4081	4140	0.99(15)				
813.9	878	2905	3092	0.94(16)	0.94(13)	$18^+ \rightarrow 16^+$	2	4321.5
	664	4714	5118	0.92(12)				
	664 + 477	10580	11194	0.95(10)				
821.1	650.5	692	1342	0.52(13)		$22^- \rightarrow 21^-$	1	5859.9

878.2	664	2474	2830	0.87(19)	0.90(15)	$20^+ \rightarrow 18^+$	2	5199.7
	664 + 477	5659	6091	0.93(12)				
907.8)[d]	724+426	2338	2649	0.88(16)		$19^- \rightarrow 17^-$	2	5275.0
948.0	404	2059	4555	0.45(7)	0.49(7)	$15^- \rightarrow 14^+$	1	3791.7
	404 + 477	4564	8095	0.56(7)				
	575 + 404	2934	6315	0.46(6)				
962.7	724+426	3278	5719	0.57(8)		$20^+ \rightarrow 19^-$	1	5351.0
970.9)[d]	426 + 724	1697	2102	0.81(19)	0.84(19)	$19^- \rightarrow 17^-$	1	5338.1
	948	1749	2044	0.86(19)				
1146.7)[d]	278+386	1836	2819	0.65(13)		$18^+ \rightarrow 17^-$	1	5123.0
1190)[d]	664+477	4768	4929	0.97(13)		$18^+ \rightarrow 16^+$	2	4697.6
1331.2)[d]	(426 + 223) + 556	2835	4842	0.59(12)		$2^+ \rightarrow 5^-$	3	1757.2

)[f] the values in parentheses are uncertainties associated with the values.

)[d] new transition energies.

)* see text for details.

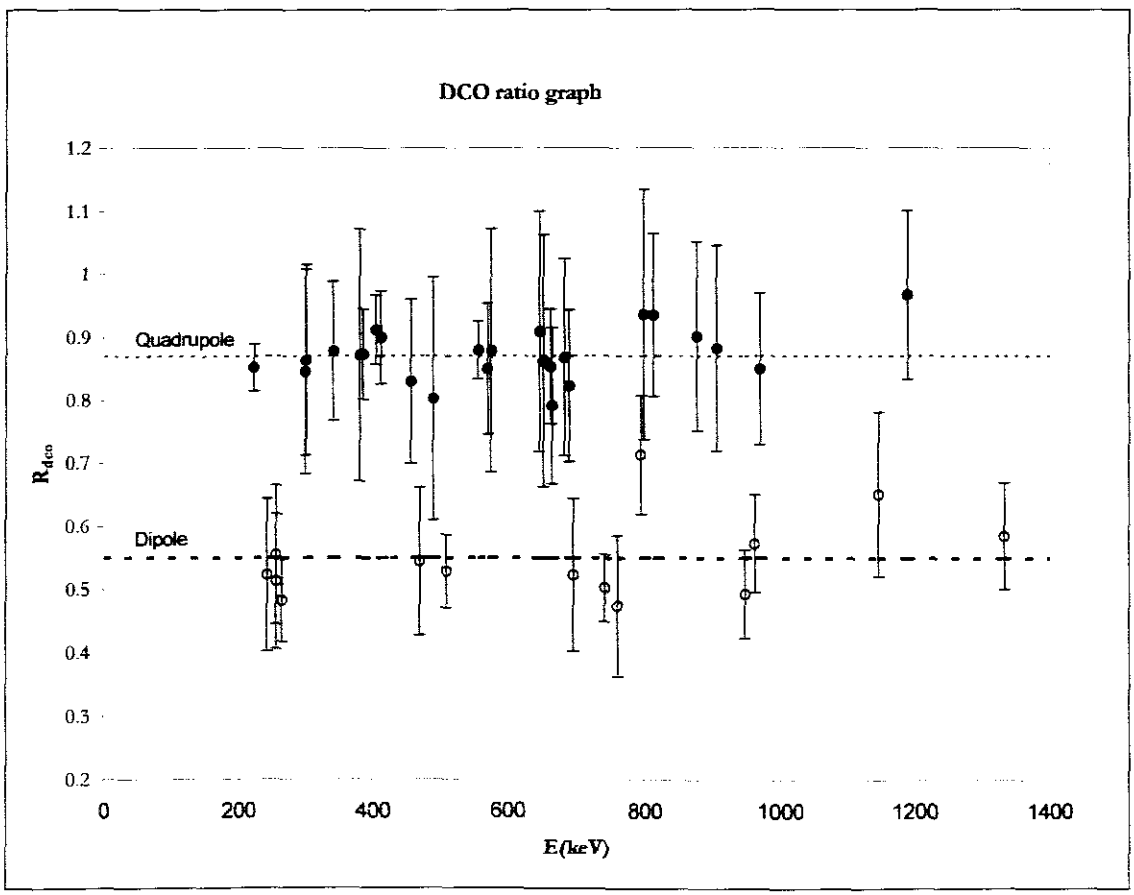

Fig 4.6: shows the relationship between γ-ray energy and R_{DCO}. *The measured averaged* R_{DCO} *ratios for dipole and quadrupole transitions are shown with dash lines.*

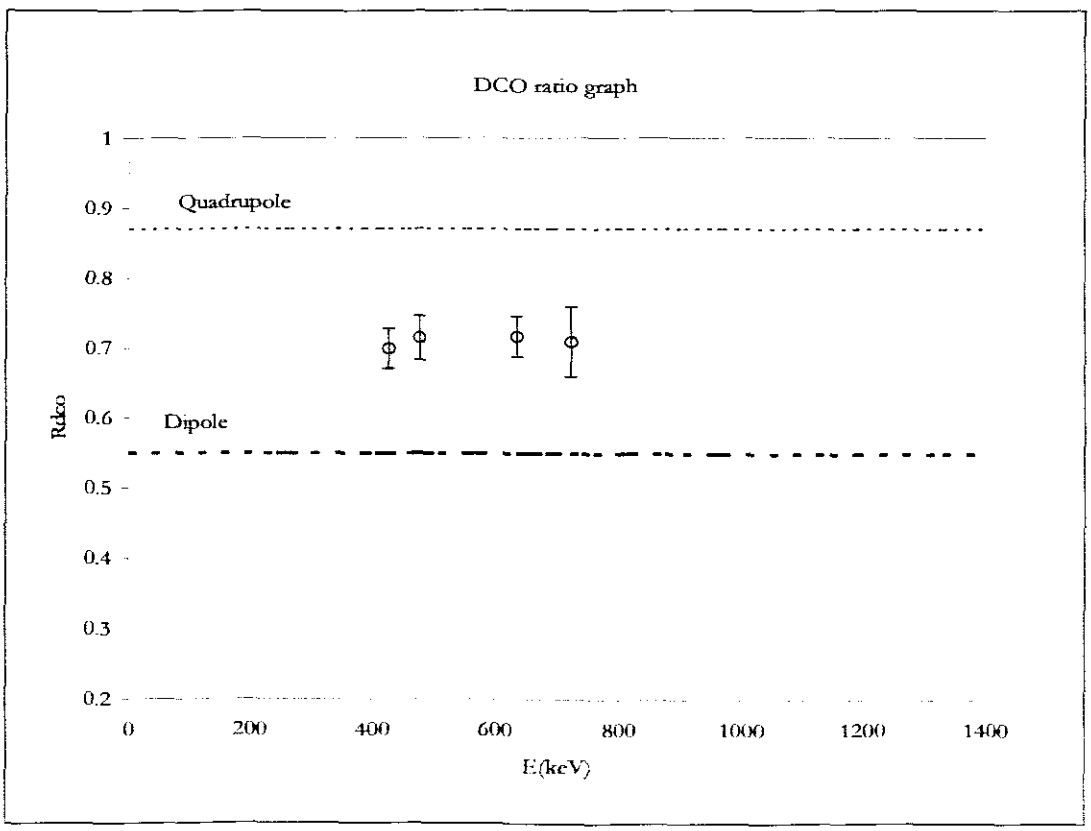

Fig 4.7: illustrates the measured values of R_{DCO} that behave in a strange way, the fact that they were previously determined [MEH91] to be pure stretched quadrupole but in this work we referred them as intermediate quadrupole.

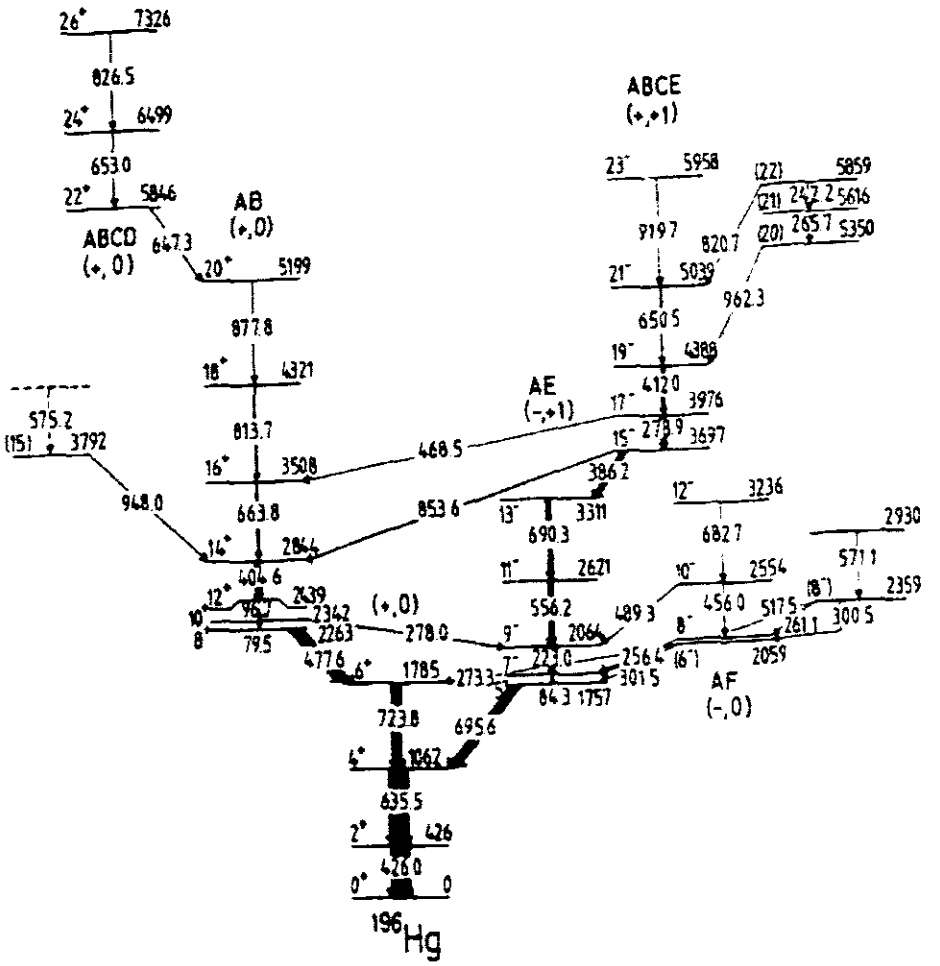

Fig 4.8: shows energy level scheme from previous work by Mahte et al.[MAH91].

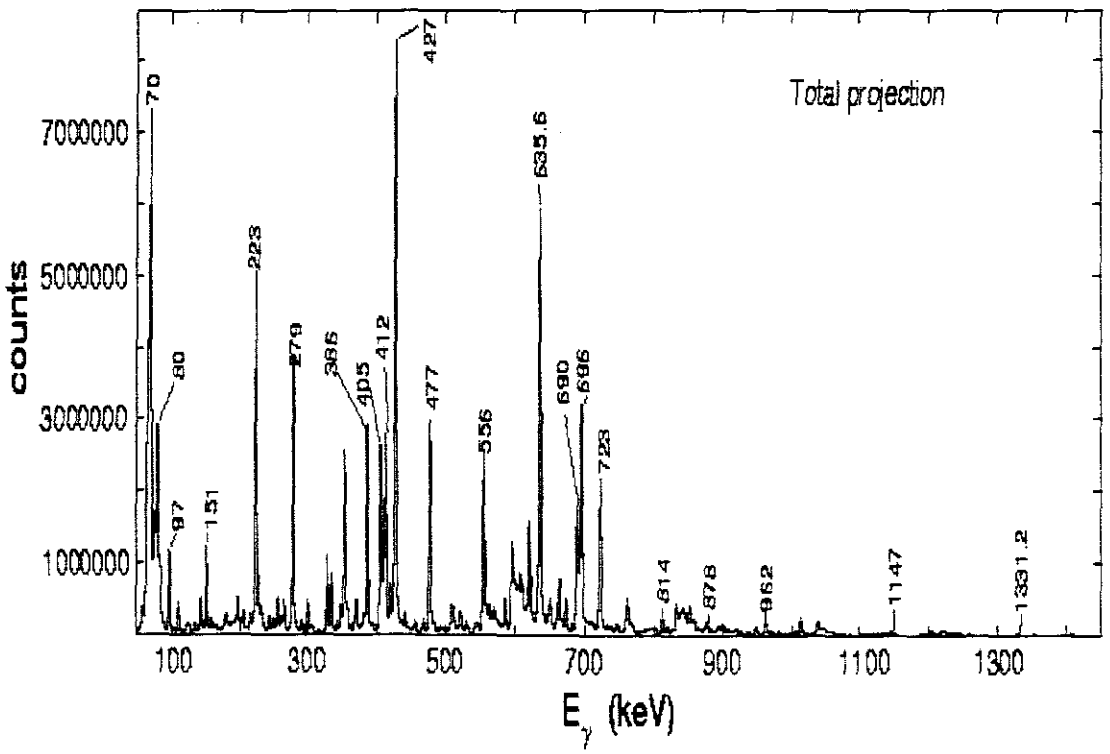

Fig 4.9: shows the total projection spectrum extracted from online matrix.

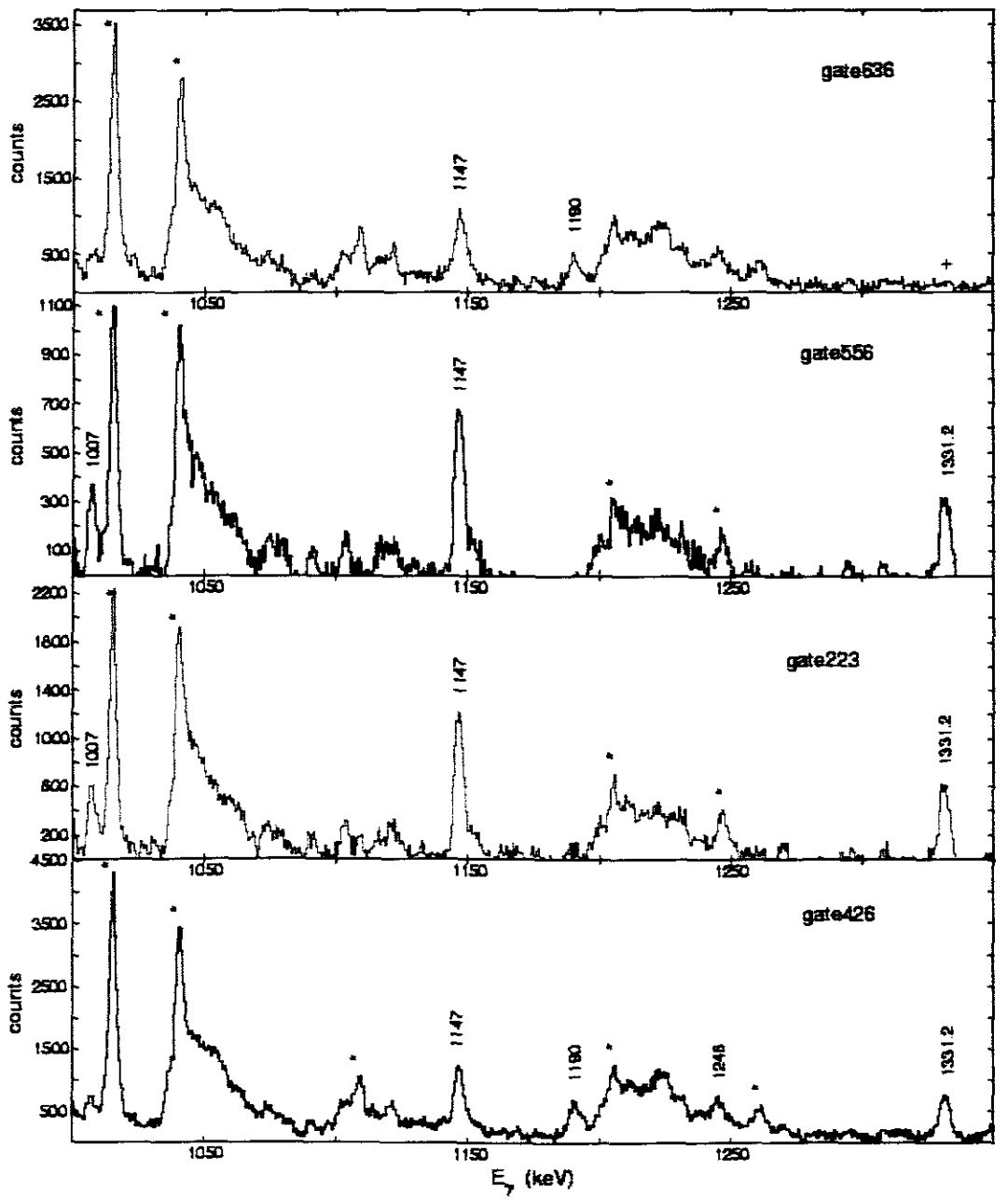

Fig 4.10: illustrates the number of peaks that are in coincidence with 1331.2 keV together with those which are parallel to this transition. The peaks that are marked with stars are not known in ^{196}Hg spectra.

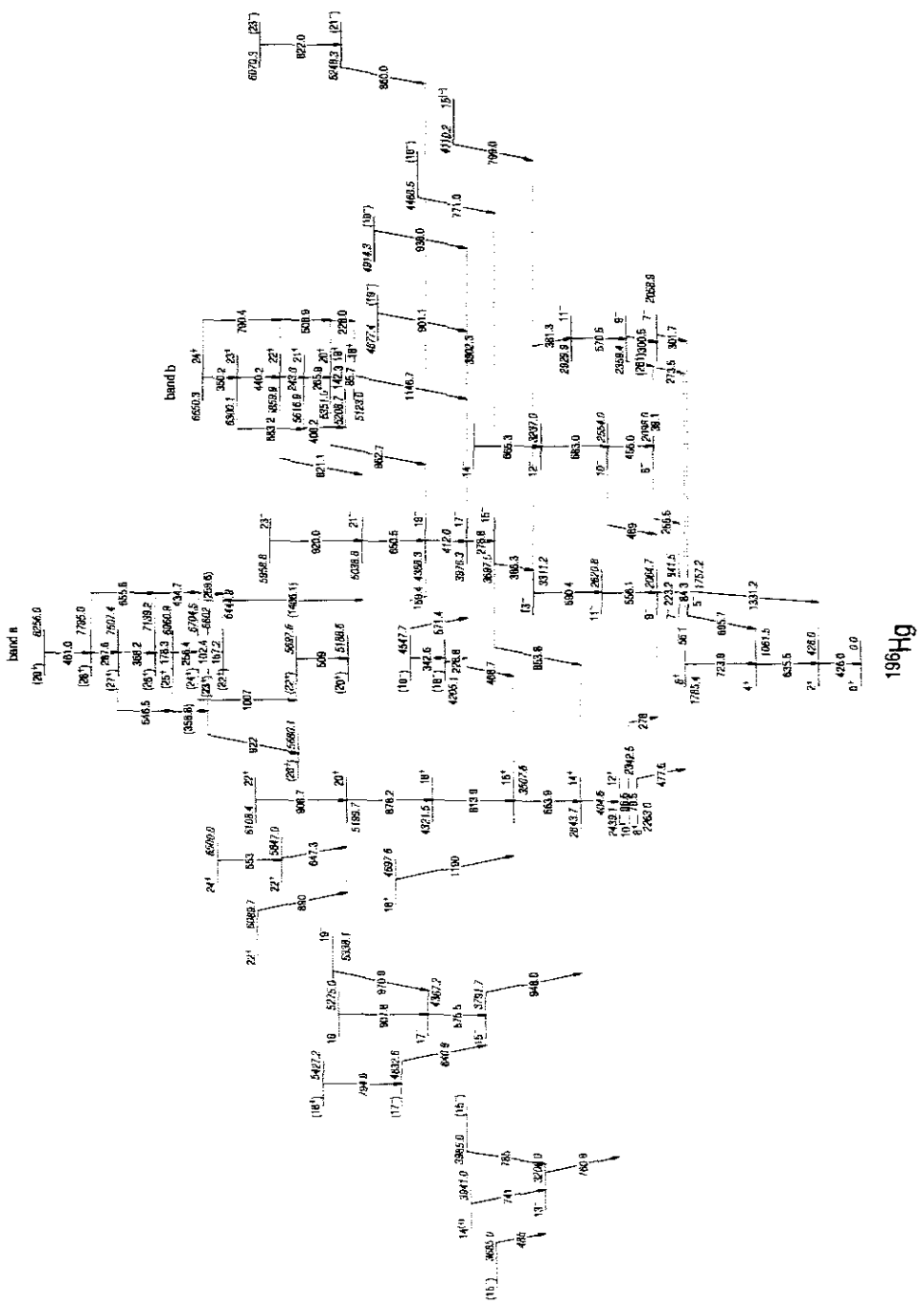

Fig 4.11: *shows the partial level scheme of ^{196}Hg energy levels are [LAW06] while spins and parities are from the present work.*

4.2 Discussions

The energy level scheme proposed by Mehta *et al.*, has been extended with the addition of a number of new levels. The two dipole bands (*band a* and *band b*) have been observed in the present level scheme as shown in fig 4.11. Such "oblate" structures have been observed in some lead [FAN91, KUH92, CLA92a, WAN92, CLA92, BAL92a, and BAL92] and mercury isotopes [CED93, COZ94, FOT96, and ROY93]. These band members are connected by M1 transitions with weak crossover E2 transitions. In many cases linking these bands with the known low-lying yrast structures is not simple due to low statistics.

4.2.1 Band a

This band was first observed by Cederwall *et al.*, [CED93] in ^{196}Hg showing the characteristics of a $\Delta I=1$ rotational band with a moderate, almost spin-independent signature splitting. In this work we have observed the same band up to the tentatively assigned 29^{+} state. We observe a 1406.1 keV transition that links lowest level of this band to the negative parity sequence, probably to the 21^{-} state at 5038.8 keV, as was done in ref [CED93]. The tentative assignment of transitions 1406.1 keV as the direct linking transitions to the previously known structures plays a role in assignment of spins and parities to the dipole band. The multipolarity of this transition could not be established but assuming it to be an E1 the lowest level in the band is tentatively assigned spin and parity of 22^{+}. The decay out of the band is fragmented and some strength also goes via a 922 keV and a 1007 keV transitions originating from the (23^{-}) and (24^{+}) levels.

It was possible to measure the DCO ratio and polarization for the 256.7 keV transition establishing it as a M1. We were however not able to verify the multipolarity of any crossovers E2 transition due to low statistics. It can also be compared with *structure 2* in ^{194}Hg as reported by Fotiades *et al.* [FOT96] that has a similar decay into the negative parity band at 21^{-} with fragmented decay into other levels. Although spins and parities were not assigned it seems feasible that these bands could have similar excitation energies at identical spins. In Cederwall's work, dipole *band a* was compared to the similar band

observed in ^{193}Hg by [ROY93], which exhibits significantly smaller branching ratios compared with the lead isotopes. We acknowledge the conclusion grown but Cederwall *et al.* that this difference may be accounted by an intrinsic configuration built on two deformation-aligned $h_{9/2}$ protons coupled to rotation-aligned $h_{11/2}$ proton and $i_{13/2}$ neutron hole states.

4.2.2 Band b

Two transitions of band b were previously known from [MEH99]; whereas majority of these transitions are new. These transitions suggest that band could be a dipole band, consisting of ΔI=1 direct transitions and competing cross-over ΔI=2 transitions. We could determine that the 265.9 and 243.0 keV in-band transitions are M1 and that the 1146.7, 962.7 and 821.1 keV transitions are all E1. This fixes the spin and parity of the band unambiguously.

We were again not able to measure any of the E2 transition competing with M1 transitions in this band due to relatively low statistics and severe contamination. The lowest level spin of *band b* was determined to be I=18ħ at an excitation energy of E=5.1 MeV. The band is observed up to an excitation energy of E=6.6 MeV and spin of I=24ħ. These bands (*a and b*) are known as irregular type of band because their M1 transitions disobey the I(I+1) rule.

In this work, *band b* can be compared to the similar *band a* observed by Coz *et al.*, in ^{192}Hg. These two bands (*b* and *a*) look fairly similar as far as the decay into the negative parity low-lying band is concerned. However, *band a* from Coz *et al.* has negative parity while the parities of the similar band (a) from the present work are firmly assigned as positive. In addition *band a* from the present work extends down to lower spin and has lower excitation energy. The spin-parity assignment of *band b* from Le Coz *et al.* is positive and it also decay to the positive parity low-lying band.

4.2.3 New structure in ^{196}Hg

We have observed the number of new transitions above the isomeric state at $I^{\pi}=12^{+}$. The DCO ratio and anisotropy measurement for this transition ($13^{-} \rightarrow 12^{+}$) shows that it is electric dipole transition. Due to low statistics we were unable to do measurements for members of this structure. However, the spins and parities were tentatively assigned. Another new structure, was observed above $I^{\pi}=15^{-}$ at an excitation energy of E=3791.7 keV. In this study we have fixed the previously tentative spin and parity of the 15^{-} level as well at that of 17^{-} and 19^{-} states above it.

The negative parity band that was first proposed by Mehta *et al.*, as AF in Fig 4.7 was confirmed and it was extended up to $I^{\pi}=14^{-}$ by 665.3 keV transition. We also place a 381.3 keV transition above the 571.1 keV transition previously observed by *Mehta et al.* This transition links up with the 13^{-} state at 3311 keV. However this placement required a change in the tentative spin assignments. In this work we determined that both the 301.7 and 300.5 keV transitions have electric quadrupole character. This implies that the level at 2059 keV has spin and parity of 7^{-} and therefore is likely to belong to a new negative parity band consisting of 300.5, 570.5 and 381.3 keV transition (all measured to be quadrupole transitions) that link up to the 13^{-} state at 3311 keV. The proposed the 39.1 keV transition that linked the 8^{-} to 7^{-} levels is so difficult if not impossible to see in γ-rays spectra and was not observed.

There are many other new transitions that were observed in this study that are known to be a quadrupole and dipole transitions that feed to the main structure, e.g. 1190 keV, 771 keV, 799 keV. In some of these transitions, we were not able to extract any information about them but others were confirmed.

CHAPTER 5 CONCLUSION AND OUTLOOK

5.1 Conclusion

The spins and parities that were tentatively assigned previously were fixed in this work. The γ- γ coincidence data analysis confirms the previously known levels of ^{196}Hg [HEP83, and MEH91] however some of the transitions were rearranged through DCO ratios and anisotropy polarization measurements. Unfortunately other transitions that were previously observed were not observed in the present work due to severe contaminations and the lack of enough statistics. The bands that are displayed in our level scheme of ^{196}Hg in the present work are (i) even-even ground state band between $I=0^+$ to $I=6^+$ transitions, (ii) evidence of decoupled bands dominate our level scheme, and (iii) dipole bands were observed at higher energies and spins labelled as band (a) and (b). The dipole bands that were observed in our level scheme are both irregular in their energy spacing. The spins and parities of *band b* were successful assigned.

Directional **C**orrelation of **O**riented states ratio measurements for quadrupole transitions that are below the nanosecond isomeric state e.g. $I^{\pi}=10^+$, 12^+ are consistently ~0.71±0.03. Although they were previously measured to be a pure stretched quadrupole, we measured DCO ratios between the average dipole and quadrupole values.

5.2 Outlook

The theoretical description of all the observed bands and structures in the ^{196}Hg level scheme need to be done. The application of the **C**ranked **S**hell **M**odel (CSM) would be appropriate for the interpretation of experimentally measured results. The cranked shell model was previously applied to mercury isotopes that include ^{196}Hg and a good description of experimental results was obtained. The relative intensity measurements will also be important for this work to make sure that there are no other unobserved transitions.

The comparison of the present ^{196}Hg nucleus dipole bands with the other neighbouring isotopes nuclei with similar bands e.g. ^{192}Hg should be accompanied by the calculations of dynamic moment of inertia ($\mathcal{J}^{(2)}=\Delta I_x/\Delta\omega$) in $\hbar^2/MeV$ units, branching ratios $B(M1)/B(E2)$ in $(\mu_N/eb)^2$ units and mixing ratios derived from the DCO ratio measurements.

REFERENCES

[BAL92] G. Baldsiefen *et al.*, Z. Phys. (in press).

[BAL92a] G. Baldsiefen *et al.*, Phys. Lett. **B275**, 252 (1992).

[BEN79] R. Bengtsson *et al.*, Nucl. Phys. **A327**, 139 (1979)

[BRI91] M.J. Brinkman, PhD Thesis, Rutgers University, (1991).

[CED93] B .Cederwall *et al.*, Phys. Rev. **C47**, 2443 (1993).

[CLA92] R.M. Clark *et al.*, Z. Phys. **A342**, 371 (1992).

[CLA92a] R.M. Clark *et al.*, Phys. Lett. **B275**, 247 (1992).

[COZ94] Y. Le Coz *et al.*, Z. Phys. **A348**, 87 (1994).

[DUC99] D. Duchêne *et al.*, Nucl. Instr. And Meth. **A432**, 90 (1999)

[FAN91] B. Fant *et al.*, J. Phys. **G17**, 319 (1991).

[FER65] A. J. Ferguson, "*Angular Correlation Methods in Gamma-Ray Spectroscopy*", North-Holland Publishing Co., Amsterdam (1965).

[FOT96] N. Fotiades et al., Z Phys. A354, 196 (1996).

[GIL95] Gordon Gilmore and John D. Hemingway, "*Practical Gamma-ray spectrometry*" (1995).

[GRE99] Paul Thomas Greenlees, PhD Thesis, Department of Physics, University of Liverpool (1999).

[GUE04] E. Gueorguieva *et al.*, Eur. Phys. J **A20**, 47 (2004).

[GUE99] E. Gueorguieva *et al.*, PhD Thesis, University Paris XI Orsary (1999).

[GUT82] M. Guttormsen *et al.*, Nucl. Phys. **A380**, 502 (1982).

[GUT83] M. Guttormsen *et al.*, Nucl. Phys. **A389**, 119 (1983).

[HEL83] H. Helppi *et al.*, Phys. Rev. **C28**, 1382 (1983).

References

[ING54] D.R. Inglis *et al.*, Phys. Rev. **96**, 1059 (1954).

[ING56] D.R. Inglis *et al.*, Phys. Rev. **103**, 1786 (1956).

[IZO03] Olga Izotova, MSc Thesis, Department of Physics, Division of Nuclear Physics, Lund University, (2003).

[JON95] P.M. Jones *et al.*, Nucl. Instr. and Meth. **A362**, 556 (1995).

[KEE99] Alex Keenan, PhD Thesis, Department of Physics, University of Liverpool (1999).

[KNO99] G.F. Knoll in "*Radiation Detection and Measurement*" Third Ed. John Wiley and Sons/New York, (1999).

[KOM04] F.S. Komati, MSc Thesis, University of North West, (2004) unpublished

[KRA88] Kenneth S. Krane, "*Introductory Nuclear Physics*", Wiley and Sons, Co, New York (1988).

[KRÄ89] A. Krämer-Fleden *et al.*, Nucl. Instr. and Meth., **A275**, 333 (1989).

[KRO81] R. Kroth et al., Phys. Lett. **99B**, 209 (1981)

[KUH92] A. Kuhnert *et al.*, Phys. Rev. **C46**, 319 (1992).

[KUH92a] A. Kuhnert *et al.*, in Proceedings of the International Nuclear Physics Conference, Wiesbaden, edited by P.Kienle and R. Block , (1992) unpublished.

[LAW06] J. J. Lawrie and E. A Lawrie; private communication.

[LIE78] R.M. Lieder *et al.*, Adv. Nucl. Phys. **10** (1978) p1.

[LIL01] J. Lilley, Nuclear Physics, "*Principles and Applications*", John Wiley and Sons Ltd, Chimchester (2001).

[MAB03] G.K. Mabala, PhD Thesis, Department of Physics, University of Cape Town, (2003) unpublished.

[MAS05] J. Masuret and J.J. Lawrie, iThemba LABS internal report, (2005) unpublished.

[MCC84] E.R. McCliment Physics Harcourt Brace Jovanovich Publisher (1984).

[MEH91] D.Mehta *et al.*, Z, Phys. **A339**, 317 (1991).

[NDT00] http://www.ndt-ed.org (photoelectric effect image).

[NEW98] R.T. Newman *et al.*, Balkan Physics Letters Special Issue 182-190 (1998).

[NIL95] Nilsson and Ragnarsson "*Shapes and Shells in the Nuclear Structure*" Cambrige University press (1995).

[OLN75] J. W. Olness *et al.*, Phys. Rev. **C11**, 110 (1975).

[PET68] R. F. Petry *et al.*, Phys. Rev. **174**, 1441 (1968).

[PET92] L. Peter Ekström *et al.*, Nucl. Instr. and Meth. **A313**, 421 (1992).

[PRO74] D. Proetel *et al.*, Nucl. Phys. **A231**, 301 (1974).

[RAD98] http://radware.phy.ornl.gov/esclev/esclev.html (1998).

[RAM06] T.M. Ramashidzha, MSc Thesis, Department of Physics, University of the Western Cape, (2006) unpublished.

[ROU01] D.G. Roux, PhD Thesis, Department of Physics, University of Cape Town, (2001) unpublished.

[ROY93] N. Roy *et al.*, Phys. Rev. **C47**, 930 (1993).

[SCH98] G.J. Schmid *et al.*, Nucl. Instr. and Meth. **A417**, 95 (1998).

[SIG01] B. Singh *et al.*, Department of Physics and Astronomy, McMaster University, (2001).

[STE75] R.M. Steffen and K. Alder, "*The Electromagnetic Interaction in Nuclear Spectroscopy*", Ed W.D. Hamilton, (1975).

[VAN89] V.R. Vanin *et al.*, Nucl. Instr. and Meth. **A284**, 452 (1989).

References

[VYM03] P.A. Vymers, MSc Thesis, Department of Physics, University of the Western Cape, (2003), unpublished

[WAN92] T.F. Wang *et al.*, Phys. Rev. Lett. **69**, 1737 (1992).

[YAM67] T. Yamazaki *et al.*, Nucl. Data **A3**, 1 (1967).